2010

The Effects of GaAs substrate miscut on InAs quantum dot optoelectronic properties: Examined by photoreflectance (PR) and deep level transient spectroscopy (DLTS)

Joanne Okvath

The Effects of GaAs Substrate Miscut on InAs Quantum Dot Optoelectronic Properties: Examined by Photoreflectance (PR) and Deep Level Transient Spectroscopy (DLTS)

by

Joanne Okvath

A Thesis Submitted

in Partial Fulfillment

of the Requirements for the Degree of

Master of Science

in

Electrical Engineering

Approved by:

Prof. _____

Dr. Sohail Dianat (EME Department Head)

Prof. _____

Dr. Seth M. Hubbard (Thesis Advisor)

Prof. _____

Dr. James E. Moon (Thesis Committee Member)

Prof. _____

Dr. Michael A. Jackson (Thesis Committee Member)

Department of Electrical and Microelectronic Engineering

Kate Gleason College of Engineering

Rochester Institute of Technology

Rochester, NY

July 2010

The Effects of GaAs Substrate Miscut on InAs Quantum Dot Optoelectronic Properties: Examined by Photoreflectance (PR) and Deep Level Transient Spectroscopy (DLTS)

by

Joanne Okvath

To my family and the ever-supportive
Jonathan Bacharach.

Acknowledgements

I would like to acknowledge Dr. Seth Hubbard for his dedicated time and effort guiding my thesis work, including pivotal input regarding the optical and electrical tests studied. Secondly, I thank Dr. David Forbes for his prompt response to my questions and priceless assistance with material growth. Also, Dr. James Moon has been an excellent resource as a professor and committee member; his courses immeasurably improved my comprehension of the material and devices examined. Finally, I thank Dr. Michael Jackson for his help as a committee member and as a professor.

I am deeply grateful to Mr. Christopher Bailey and Mr. Stephen Polly for their guidance and support throughout my research work. Also, Ms. Chelsea Plourde and Mr. Zachary Bittner provided valuable services with regards to device fabrication. Dr. Stefan Preble and Mr. Karthik Narayanan also provided various helpful advice and loaned equipment that assisted in the completion of this work. I would also like to thank Dr. Brian Landi for introducing me to NanoPower Research Labs (NPRL) and facilitating my start at NPRL as a graduate research assistant.

The optical and electrical characterization tests would not be possible without the use of equipment in the Photovoltaic Characterization Lab maintained by NPRL and supported by these organizations: the US Government, National Science Foundation (Grant #DMR-0955752), and US Department of Energy (Grant #DE-FG36-08GO18012). Growth and characterization support provided by NASA Glenn Research Center through Grant #SAA3-844.

Abstract

In this work, advanced III-V quantum dot (QD) materials are discussed and examined theoretically. The significance of substrate miscut with regards to QD growth is discussed and previous experimental data are examined to show established trends with regards to favorable miscut degree. In order to examine the miscut effect further, multiple testing techniques are presented which characterize material quality as it pertains to optoelectronic device performance, including optical and electrical spectroscopic methods.

The optical probing techniques of photoluminescence (PL) and photoreflectance (PR) are used to experimentally characterize the optical properties of GaAs baseline and InAs/GaAs one-layer QD samples. Experimental results reveal conclusive trends concerning QD energetic transitions and material quality as it relates to substrate miscut.

Deep level transient spectroscopy (DLTS) was investigated as an experimental method to inspect possible non-radiative defects or other QD defect properties which may contribute to PL signal degradation in miscut samples. Included in the DLTS evaluation section, *I-V* and *C-V* analyses are presented to pinpoint deep traps for profiling, as well as obtain general material parameters and trends. The deep defect profiling suggests differences between miscut samples.

The behavior of the reduced PL signal, corresponding to reduced radiative-recombination in certain miscut samples, is discussed as related to the compilation of data obtained through optical and electrical probing.

Table of Contents

Table of Figures

.

Chapter 1

Introduction

Epitaxial growth of semiconductor superlattices, or man-made semiconductor crystals, has been investigated since the 1970s as a venue of improvement for solid state devices. Termed low dimensional structures, the size of the semiconductor crystal formed is comparable with interatomic distances on the nanometer scale, thus popularly referred to as nanostructures. The electronic properties of nanostructures are different from bulk single-crystalline material in that they are influenced by quantum effects[1]. The quantum limitations (confinement) produced by these nanostructures - dependent on their size and shape - changes the spatial overlap of electrons in the conduction and valence bands, directly related to the transition energies and strength of optical transitions observed[2]. These properties favor a growing generation of enhanced electronic devices with precisely engineered optoelectronic properties[1,2].

Semiconductor material epitaxially grown by monolayer, or a single layer of atoms, allows the control of the underlying physics governing nanostructure formation and has become the foundation for advanced optoelectronic devices such as high-performance lasers, LEDs, detectors, solar cells, *etc*. Nanostructures with enhanced carrier confinement - where increased confinement results in structures such as quantum wells (QWs) (two-dimensional), quantum wires (QWRs) (one-dimensional) or quantum dots (QDs) (zero-dimensional) - allow greater spatial precision in device engineering[2]. Recent research efforts involving semiconductor device improvement using nanostructures includes: QW infrared cascade detectors in the AlGaAs/GaAs

material system operating at 90 K and above[3], nanowire superconducting field-effect transistors[4], and QD radiation sensors based on ZnO and CdTe exhibiting excellent stability under photon irradiation[5].

1.1 Quantum Dot Devices

In QWs, electrons are confined to a two-dimensional layer between high bandgap semiconductor layers providing a space where electron energies and thresholds for excitation are customized by changing the well thickness. Carriers in QWRs are confined to movement along the one-dimensional wire axis, and in QDs the carrier can experience no free motion or very limited motion[2]. In the mid-1980s, the potential of QDs to outperform QWs and QWRs was recognized as their unique optical properties were further explored. QDs experience reduced phonon scattering, longer carrier lifetime, and lower detector noise (from zero-dimensional confinement)[6]. Also, the possibility of isolating single photon emission from QDs, the potential to manipulate the spin state of carriers, and other novel properties continue to be scrutinized in many semiconductor device fields[1]. In the following section, a brief overview of the potential and realized device applications for epitaxially-grown QD structures will be presented that includes the most prominent fields of QD technology (although many other QD semiconductor applications exist) such as state-of-the-art lasers, light-emitting diodes, detectors, and solar cells.

1.1.1 Lasers

The QD laser ideal model is made up of an array of uniform spherical shapes in the QD layer encompassed by a higher bandgap material to confine carriers[7].

Advantages of the QD laser system originate from the increasing density of states while electron dimension travel is limited[8]. QD laser operation is workable due to the QD heterostructure that exhibits positive gain for high carrier injection levels[9]. QD lasers have been in development since 1993, and Kirstaeder *et al.* presented the Fabry-Perot injection laser in 1994 using embedded InGaAs/GaAs QDs[9]. QD laser research since has involved the realization of predicted improvements in laser performance, such as temperature-insensitive threshold currents and increased modulation speed[10]. Many QD laser advancements have been realized, including high power performance, relaxed cooling requirements, and improved wall-plug efficiency[9].

In 1996, Singh identified the QD inter-sublevel optical transitions as candidates for developing an advanced infrared (IR) laser, and Vorob'ev *et al.* reported the pronounced enhancement of spontaneous far IR emission in a near IR QD laser[9]. Mid-IR emission from QD lasers has since out-performed their QW counterparts by an order of magnitude[7]. More advanced applications include using QDs in vertical cavity surface emitting lasers (VCSELs) for fiber optic communications and auspicious results have been observed for 1.3 μm lasers on GaAs substrates[8]. A world-record threshold current density for a laser was reached in 2000 at 19 A/cm^2 [8] and ultrahigh material gain as well as suppression in gain saturation has been developed[7].

1.1.2 Light Emitting Diodes (LEDs)

QD structures were first introduced as LEDs in a GaInAsP/InP system[9]. QDs aid the construction of miniature, single or multicolor LEDs with high luminous efficiency, that are lower in cost and weight[11]. Zhang *et al.* produced ZnSe and CdTe QDs for blue, green and red emission in 2008[11]. Also, vertically aligned, electronically coupled QDs

are used in research, including studies done by Solomon *et al.*, as the active region in LEDs operating at room temperature[12]. The broad emission and gain characteristics in QDs can produce superluminescent LEDs (SLEDs) as well[10]. Advanced research also involves spin QD LEDs where radiative recombination in the LED's active region follows radiative selection rules, driven by the injection of spin-polarized carriers.

1.1.3 Detectors

QD detectors reside on the inverse side of the above LED discussion. Single QD photodiodes have demonstrated resonant optical excitation in the QD ground state (or the state closest to the valence band) and photocurrent detection is possible[13]. QD IR detectors (QDIPs) have been realized as another device application, and are found to be high-performing detectors due to reduced phonon scattering, higher temperature operation, and lower dark current[14]. In future research and proposals put forth by Phillips *et al.*, QDIPs are expected to achieve the highest IR detector performance[15].

1.1.4 Solar Cells

QDs are an exciting research field in advanced solar cell technologies, as the precise control of the nanoparticle size allows bandgap tuning or engineering (taking advantage of the near-infrared and infrared solar spectrum)[22]. Typical *III-V* single-junction photovoltaics (PV) absorb only a portion of the available spectrum in space, and theoretical efficiency limits have been developed by Shockley and Queisser of 33% for single material absorbers[22]. QDs can enhance the performance of solar cells by introducing sub-host states into the band structure that act as separate effective bandgaps[20]. Their existence allows the material to absorb lower energy (higher wavelength) photons available from the solar spectrum, which would otherwise optically

pass through the host material. This should theoretically increase the number of carriers collected. Particularly in GaAs solar cells, the limiting bandgap is about 1.42 eV or 870 nm, thus any photons below this energy would not be converted into electronic power.

Furthermore, crystalline *III-V* materials stacked in series, called a tandem or multijunction design, have been analytically scrutinized in detail and are currently in wide use as an improvement to the single junction solar cell[16,17]. These tandem designs, however, are current-limited by the cell producing the lowest short-circuit current (typically the GaAs layer in the popular InGaP/GaAs/Ge system), and QD introduction has been demonstrated to increase the limiting short circuit current by 8%[18,19]. Also, the existence of multiple bandgaps available for capturing lower energy photons due to QD formation[20] has been shown to enhance current in concentrator PV[21], where the photonic energy available from the sun is concentrated to several hundred times its original intensity on to a small area of PV material.

Another theoretical solar cell design has been dubbed the intermediate bandgap solar cell (IBSC) and was first examined by Martin and Luque in 1997[22,24]. The introduction of an intermediate band (IB) in the forbidden gap of the host material is the foundational concept for the IBSC. This IB concept is an extension of the impurity effect in semiconductors, where impurities are brought close enough so their wavefunctions overlap into a continuum[22,24]. As seen in Figure 1, this state within the material allows the absorption of less-energetic photons by adding two different energetic pathways for the electron - from valence band (VB) to IB and from IB to conduction band (CB) - and can thus assist electrons to the conduction band using NIR or IR light[22]. The setup seen in Figure 1 thus reduces the loss experienced by a single-junction solar cell.

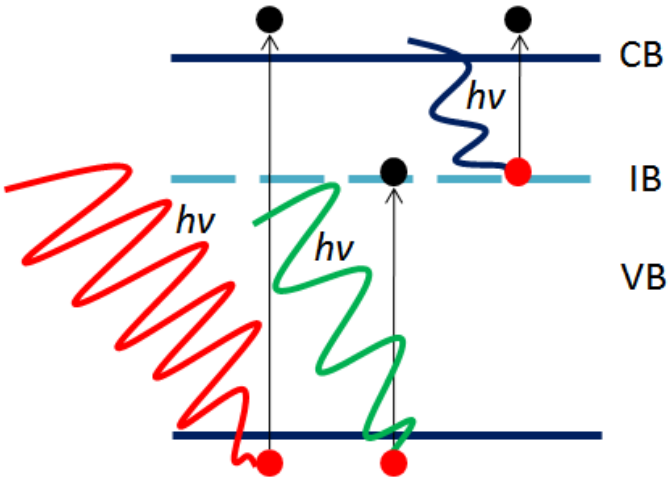

Figure 1: The intermediate band solar cell (IBSC) concept illustrated: the material makes use of photonic energy that would not be absorbed by the host bandgap by using an intermediate band (IB) which assists electrons to the CB.

The ideal band structure for this material can be derived from a detailed balance model for the current produced from each absorption process while considering the spectral flux incoming to the cell[22]. Solving for the energy band separations so as to maximize efficiency, these ideal bandgaps (for light that is not concentrated) are as follows: conduction to valence band (VB) separation, E_{CV} (a host material bandgap) of 2.41 eV, a valence to intermediate band separation, E_{IV} of 1.49 eV, and an intermediate to conduction band separation, E_{CI} of 0.92 eV[22,23]. The maximum theoretical efficiency under these conditions is 46.8%[22]. Progress toward a material realization of the IBSC continues since the introduction of this concept, and QDs have been identified as a realizable solution[22,24].

With periodically spaced QD arrays, tunneling between the dots becomes a higher probability. This tunneling electron transfer could form the effectively continuous intermediate band as envisioned by Marti and Luque[39]. The bandgap properties of the InAs/GaAs QD system are very well understood and have been widely used to test the

IB concept[23], but the energy transitions of this system are not ideal (with E_{VC} of 1.42 eV, E_{IV} of ~1.00 eV, and E_{CI} of ~0.30 eV). Well-controlled growth behavior of this system, however, allows the study of possible optimizations toward realizing the IBSC[23]. NanoPower Research Labs has completed extensive research in the study of these crystalline PV materials, including optimizations involving the InAs/GaAs QD system, thus the bulk of this work will concern this specific QD structure.

1.2 Theory and Growth of Nanostructures and Quantum Dots (QDs)

In device applications, the uniformity and size of QD arrays is of prime importance with regards to high quality and performance. To achieve high functionality and precisely-controlled QD energy states, however, a solid understanding of the quantum effects in QDs is required. Equally significant to device operation is the integrity of QD formation as affected by various growth techniques for these heterostructures.

1.2.1 Theory

A heterojunction forms when two different semiconductor materials are put in contact. A special case of a repetitive semiconductor heterojunction is a heterostructure, where a thin layer of narrow bandgap material is placed between two layers of wider bandgap material. If the width of the narrow bandgap layer is sufficiently small, quantum properties begin to emerge in the structure[25]. Since the late 1950s, the use of such ultra-thin layers to produce quantization effects has been continuously investigated[9].

Quantum properties mostly refer to the existence of discrete energy states where an electron may reside below the continuum of unconfined bulk states[2]. As discussed

earlier, lower dimensional structures (where dimensionality refers to the degrees of freedom in electron momentum) exhibit characteristics much different from that of bulk semiconductor material. These lower dimensional structures produce quantum confinement effects due to their dimensions being smaller than the Bohr exciton radius (on the nanometer scale)[22], and are thus named nanostructures. Thus, quantum confinement limits electron-hole Coulomb properties as well as single-particle density of states; electron-hole binding increases with confinement so thermalization effects are weaker and discretized transition energies may be engineered and are dependent on the nanostructure size[2].

Nanostructures may confine electron movement to two dimensions (QWs), one dimension (QWRs), or zero dimensions (QDs). In this study, the zero dimensional QD case is explored, as the many state-of-the art optoelectronic applications' success depend on the uniformity and controllability of QD properties (as outlined in the section above). The size limitations for a spherical QD at room temperature are dictated by a critical diameter, D_{min} so that at least one discrete energy level exists, as shown below[9],

$$D_{min} = \frac{\pi\hbar}{\sqrt{2m_e^*\Delta E_c}} \qquad \text{Equation 1}$$

where ħ is the modified Planck's constant, m_e^* is the electron effective mass, and ΔE_c is the conduction band offset. For an InAs/GaAs QD system, this critical diameter is typically 2 or 3 nm[22]. In typical III-V materials, the transition to strong confinement occurs when the QD diameter equals about 10 nm and weak confinement at about 100 nm [2].

A QD is often referred to an artificial atom[1], or an "atom in a cage"[9]. To better approximate the electron confinement behavior, however, the spherical representation of a QD can be simplified to that of a quantum box[26]. In a quantum box, energy sublevels exist that may be modeled using the three-dimensional Schrödinger equation where an infinite potential is assumed separating the box interior from the exterior. For the infinitely deep barrier case, the solution to this equation may be written as below,

$$E_{x,y,z} = \frac{\hbar^2\pi^2}{2m^*}\left(\frac{n_x^2}{L_x^2} + \frac{n_y^2}{L_y^2} + \frac{n_z^2}{L_z^2}\right) \qquad \textbf{Equation 2}$$

where $E_{x,y,z}$ are the energy sublevels in the QD, m^* is the carrier effective mass, L_x , L_y , and L_z are the box Cartesian dimensions, and n_x, n_y, and n_z are the three quantum numbers used to designate each energy state. From this equation, the utility of QDs in bandgap engineering is easily conveyed, where the exact energy transitions desired can be realized by customizing QD size (L_x , L_y , and L_z).

The quantum box approach is well-established as a quantification of discrete energy states in a QD, however iterative solutions to the spherically symmetric Schrödinger equation are treated elsewhere[26]. Boxes and spheres aside, real QD systems such as InAs/GaAs become much more theoretically complex. Actual QDs form as discs or pyramids and modeling of these systems includes eight-band *k•p* theory and pseudopotential approaches; these calculations are considered more accurate as they couple dispersion and strain effects[27]. The precise engineering of quantum-confined states in a QD system via theoretical treatment is not the focus of this research, however, thus the broader approximation of the quantum box will suffice as a general understanding of possible zero-dimensional energy states.

QDs are easily formed in the intrinsic region of a *p-i-n* junction[39], a semiconductor structure widely used in the device areas listed above, and a band diagram view of this system is shown below. The electrical and optical properties of QD material, such as photonic absorption abilities, change with dot dimensions as put forth in the theoretical treatment above[22]. As mentioned, a QD is a three-dimensionally confined structure, where a few discretized energy levels for electron/hole transfer appear as seen in Figure 2 below, as opposed to the much more dense availability of states in the CB of the host material[35]. An inverse relation exists between the particle size and the photon energy, *hv* it is able to absorb, *i.e.* the greater height of the dot (given the diameter meets dimension requirements as seen in Equation 1), the lower the energetic transition[28,22]. Figure 2 below depicts the band diagram of a hetero QD material and the multiple energetic transitions possible within the bandgap, E_g of the original material.

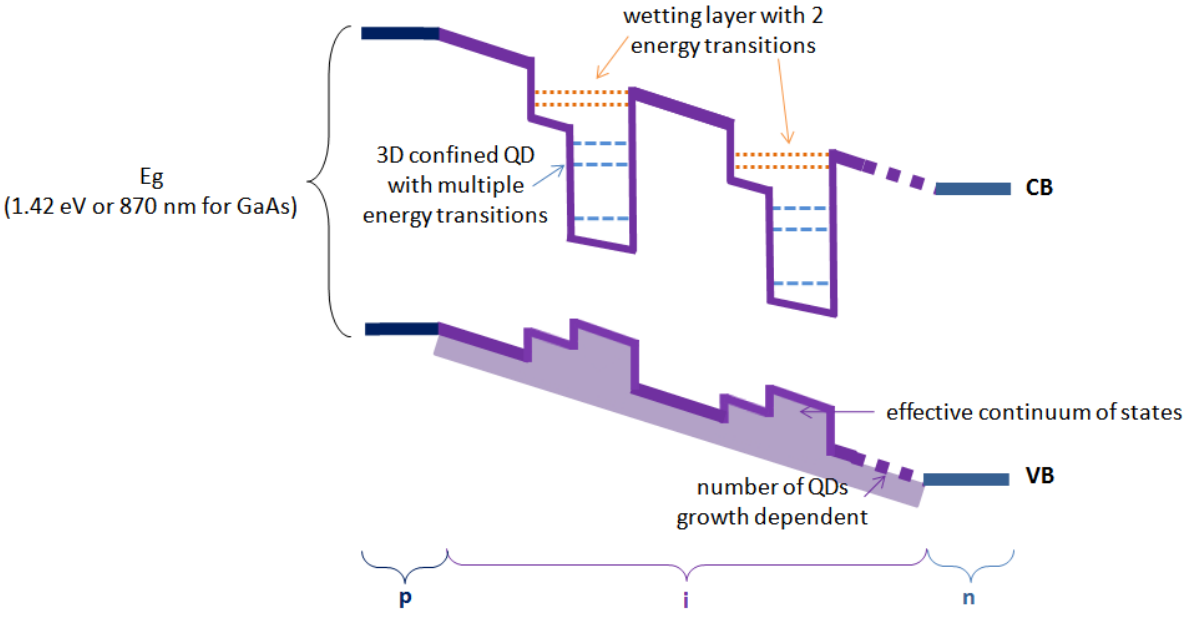

Figure 2: Band diagram showing QDs in the *i*-region of a *p-i-n* photovoltaic stack. Multiple discrete energy levels are depicted within the QD as well as the wetting layer (WL) (considered a QW). Note that a VB offset is present due to the introduction of QDs, which has been shown to cause a reduction in the device open circuit voltage.

The wetting layer (WL) depicted is treated as a QW and will discussed further in the QD growth section. An effective quasi-continuum of states is observed in the VB offset of the QDs[29] due to hole effective masses being significantly higher than that of the electron, thus according to Equation 2, confined energy levels in the VB are more closely spaced and comparable to the bulk continuum of states[30], as illustrated in the figure above. The VB offset paired with the offset from the CB of the WL may also be the cause of a reduced open circuit voltage in quantum dot solar cells (QDSCs) due to a reduction of the effective material bandgap[31]. Other material factors such as QD uniformity and the density of QDs in the intrinsic layer also affect the band-to-band transition energies[32]. From a device perspective it is usually precisely uniform and closely spaced QDs are desirable, especially in the optoelectronic applications discussed previously. These theoretical and design considerations are taken into account during QD growth to control optoelectronic material properties, as will be discussed in the following section.

1.2.2 QD growth

In general, research encompasses two different QD systems of 1) inorganic colloidal QDs made by chemical synthesis, for example CdSe, or 2) epitaxial or vapor phase-grown crystalline QDs, such as *III-V* compounds and group *II-IV* semiconductor[22]. The second group of epitaxial QD structures will be investigated in this study, due to their aforementioned device applications. Using single-crystalline molecular beam epitaxy (MBE) or metal organic chemical vapor deposition (MOCVD), precise growth of many heterostructures is possible, where abrupt interfaces allow semiconductors of different bandgaps to be sandwiched together[2]. Compared to MBE,

where gaseous elements are physically deposited by condensing them on the sample wafer, the growth of crystals in MOCVD is by chemical reaction. In MOCVD, precursor organic gas molecules are combined with the atoms of the inorganic crystalline material to be deposited and flow over a hot semiconductor wafer in a vacuum chamber[33]. The heat pyrolyzes the organic molecules leaving the desired atoms on the surface; this method is repeated layer by layer, growing thin, high quality semiconductor layers with a crystalline structure perfectly aligned with that of the substrate. Finally, by varying the gas composition, the atomic properties of the crystal may be modified. Recently, MOCVD has proven to be an excellent producer of high-quality nitrides for the best performing photonic devices, and is also deemed the most versatile technique for *III-V* and *II-IV* compounds[33], and is thus the preferred method in this study.

QDs, when grown under the correct conditions, can self-assemble into tens of billions of dots per square centimeter with high uniformity[1]. This self-ordering occurs due to an inhomogeneous state in the hetero material, where long-range strain causes the single-domain (or planar) state to be less energetically favorable, thus a multidomain state develops[9]. Several growth methods exist, but thermodynamic diffusion-driven growth methods are widely known for formation of coherent or defect-free material[9,22]. These growth modes include: Volmer-Webber, Frank-van der Merwe, and Stranski-Krastanov. Due to the higher incidence of dislocations in the first method and the two-dimensional properties of the second, the Stranski-Krastanov (SK) growth mode is used in this study.

In SK growth, crystals of slight lattice mismatch and low interfacial energy are brought together, such as Indium Arsenide (InAs) and GaAs[34,35], the materials used for

this study. QDs may also be formed by AlP, GaP, InP, InSb and GaN as well as a combination of Si and Ge[39]. The lattice constant diagram below[36] in Figure 3 illustrates the mismatch between InAs and GaAs, as well as other materials' lattice parameters. The lattice mismatch between InAs and GaAs is typically about 7%[69].

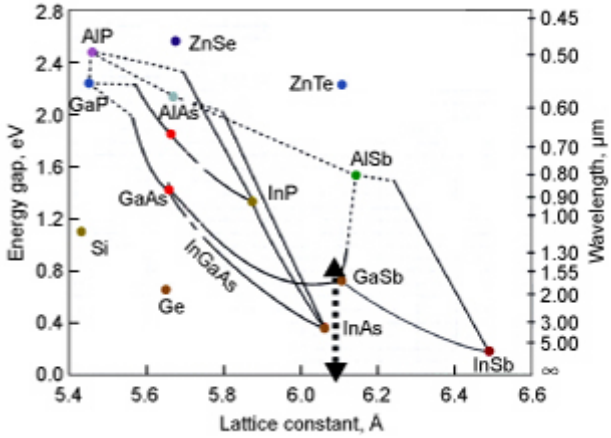

Figure 3: The crystal growers' chart showing material lattice constants dependent on energy gap in eV (or bandgap in µm) and on the ratio of materials used[36].

After an initial layer-by-layer two-dimensional type growth (InAs is typically deposited in multiples of monolayers, ML or a single layer of atoms), the strain energy between the two materials reaches a level where three-dimensional heteroepitaxial islands are more energetically favorable than planar growth[37,35]. The growth of the crystal islands results in locally developing facet edges that act as boundaries for the effective surface stress relief; thus reducing the overall surface energy of the island[35]. This spontaneous formation due to interfacial strain induces a rounded lens type shape, thus christened a QD. Their nucleation sites (where the dots prefer to appear) are periodically spaced with the least common multiple of the InAs/GaAs lattice constants[34,35]. This concept is pictured in Figure 4 where the QDs form ordered arrays

along the crystalline lattice step edges[38]. A small amount of crystalline material is needed to build up strain to form a QD, and thus leaves a thin layer of InAs below the QDs, termed the wetting layer (WL) [37,38,39]. An atomic force microscopy (AFM) image of the surface of a GaAs substrate with deposited InAs QDs is shown in Figure 4 below[38]. As QD growth methods have advanced, highly uniform and defect-free InAs/GaAs QD have been demonstrated[40].

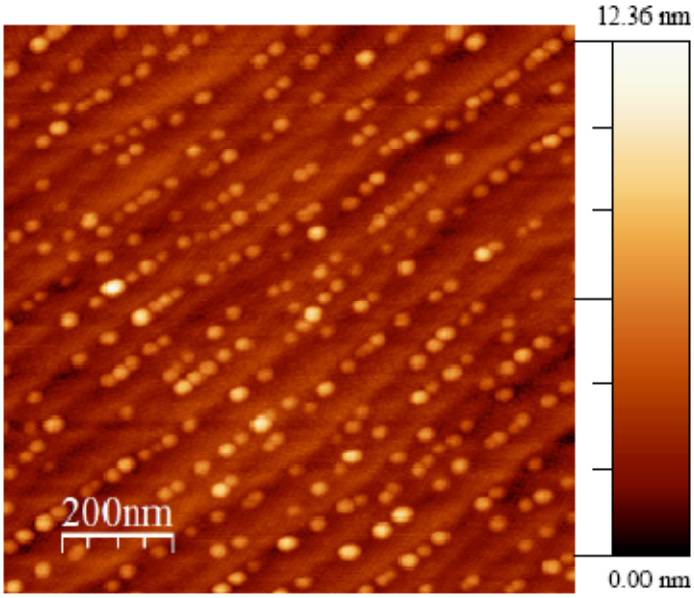

Figure 4: InAs QDs grown on GaAs substrate pictured using AFM[38]. Note the lined appearance of the substrate, which demonstrates the concept of favorable nucleation sites.

Common QD sizes range from about 4 to 20 nm in diameter[35] and 5 to 10 nm in height[39]. Dot densities range between $2x10^{10}$ cm^{-2} and $1x10^{11}$ cm^{-2} with typical size distribution of approximately 10%[7]. The size distribution of QDs upon the crystalline substrate takes a Gaussian or Lorentzian form due to formation probabilities[9,41]. Dependent on the growth conditions (such as changing nucleation sites, a topic which

will be discussed further shortly), one particular size of QD may be the most statistically favorable, with other QDs following the standard bell-shaped size distribution[42].

1.3 Substrate Misorientation (or Miscut) Optimizations

Single-crystalline GaAs has a well-defined atomic structure, forming a Zincblende lattice belonging to the tetrahedral phase, and is usually depicted as two inter-penetrating face-centered cubic lattices, as seen in Figure 5, where *a* is the lattice constant of the material[43]. The planes formed by these extremely uniform lattice surfaces have a significant effect on the material deposited above, as in the case of epitaxial growth. Miller indices define the different possible crystal planes with regards to three axes (defined with respect to the material's unit cell)[43], as seen in Figure 5 as well.

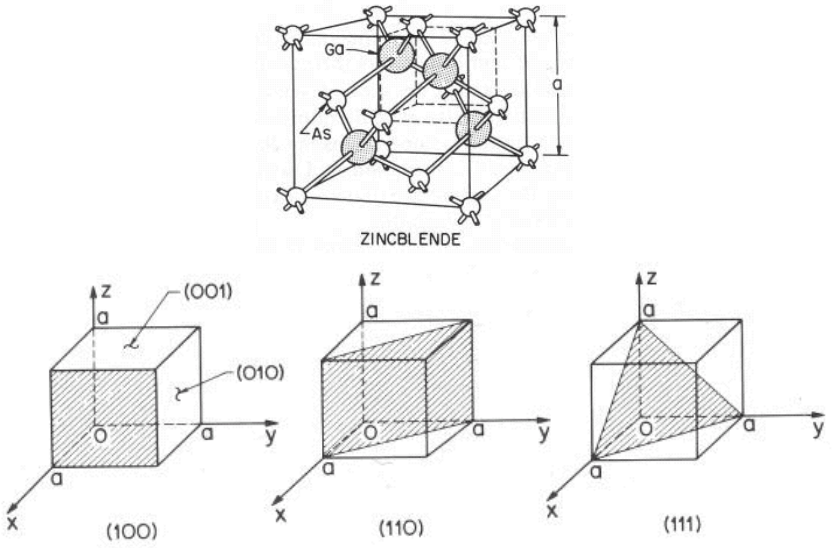

Figure 5: Top: Zincblende lattice structure of two intersecting cubic structures, one of Ga and one of As. Below: representation of miller indices used to directionally indicate crystal planes with regards to the three axes defining the material's unit cell[44].

The different planes of the Zincblende surface expose different atomic structure of the GaAs lattice; for example, the crystal surface is terminated with Ga in the (111)

plane. Once an ingot of single-crystalline material is grown, it can be cut along a precise crystal plane in order to terminate the surface of the material at Ga or As faces. Hence, substrate misorientation (or miscut) refers to the degree at which the substrate is cut from the material ingot as seen in Figure 6, which varies the atomic terraces seen on the substrate surface. Sumitomo Electric provided 2" diameter, approximately 350 μm thick, n^+-type (Si doped) GaAs substrates used in this research, and Figure 6 below provides their specifications for wafer miscut direction, where the (111') face shows the group *V* element or As and the (111) surface shows the group *III* element or Ga. A 2º cut off a (100) plane towards the [110] plane direction has been the historical choice for GaAs substrates for NanoPower Research Labs due to better quality formation of QDs[38].

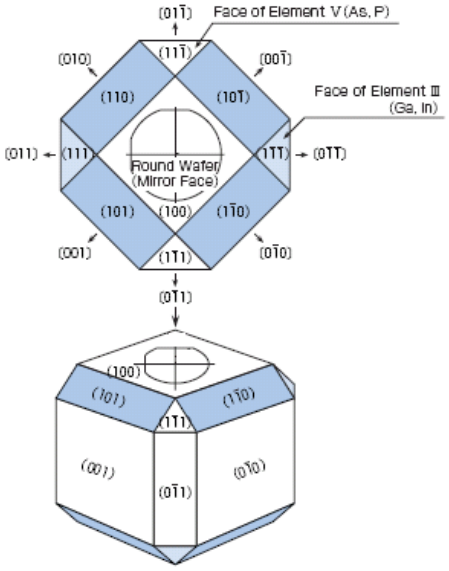

Figure 6: Depiction of substrate misorientation or miscut. The cylindrical material ingot (not pictured here) is cut at different angles from the normal (100) surface, changing the atomic step edges on the substrate.

Three different miscuts are examined in this study, a 2*K*, 6*K*, and a 6*N*. In the nomenclature used by Sumitomo, 2*K* (6*K*) means 2 (or 6) degrees off the (100) lattice toward the [110] plane. 6*N* means 6 degrees off the (100) toward [111], a Ga terminated face (see Figure 6). Since the step edges run parallel to the [011] lattice plane, these tilts change the atomic terraces on the surface of the substrate in shape and width. Incorporation of n^+-type doping in the substrate varies with miscut degree and plane, where the 2*K* miscut is Si doped between 1.10-1.18x10^{18} cm^{-3}, the 6*K* 1.43-1.66x10^{18} cm^{-3}, the 6*N* 1.24-1.36x10^{18} cm^{-3}.

Usually miscut is used as a control factor for improved surface morphology (affected by the symmetry of the crystal lattice) and electrical properties for semiconductor materials; the optimum degree and plane of the cut is highly dependent on the materials used and the full extent of miscut effects are still being catalogued and researched. Okano *et al.* found that the angle of GaAs substrate miscut varies the conduction properties of the n-type, Si doped GaAs epitaxial layer[45]. Kuech and Veuhoff found that substrate misorientation affected carbon incorporation on Arsenic surfaces[46], and substantial drops in carbon doping have been observed with increasing misorientaton from the (100) surface. This drop in carbon was attributed to the increase in atomic H on the semiconductor surface from a higher AsH_3 pyrolysis rate. Ching-Wu Wang concluded that misorientation on GaAs substrates exhibited different degrees of surface roughness, testing 3, 5, and 15 degree miscut samples[47]. The increased surface roughness (the highest in the 5 degree sample) was supposed to induce more stacking faults in the deposited epilayers, thus causing the formation of dislocations

acting as non-radiative recombination centers. Stacking faults are encompassed by dislocations, decreasing carrier lifetime and degrading most optoelectronic devices[48].

In terms of confined semiconductor structures, Lobo and Leon discovered that carrier diffusion lengths shortened and densities of grown heterostructure islands increased by an order of magnitude on miscuts on $(311)_A$ GaAs substrates[49]. Also, changes in the Al content of an AlGaAs/GaAs QW have been observed on miscut GaAs substrates, this modulated content ascribed to the large step formations on the atomic surface[50].

The primary goal in variation of miscut, with regards to QD growth, is to change the nucleation site properties, where QDs are more likely to form. Nucleation sites that are more closely spaced and precise (*i.e.* limit QD growth to one dot of a particular dimension in ordered arrays) help increase the uniformity, density, and size distribution during QD growth and thus the overall optical properties of the material can be better controlled. For example, a higher-degree miscut would theoretically increase the number of atomic step edges on the substrate's surface thus increasing the density of nucleation sites and finally QD density. As seen in previous studies, QD nucleation is energetically favorable along these steps, and strings of QDs at multi-atomic steps have been observed[51]. Increase in the concentration of incoherent QD islands and island bunching, however, on higher surface steps may be a concern[51].

Hubbard *et. al* found in numerous studies that the 2 degree substrate misorientation is in fact preferable to the 6 degree miscut as related to QD material quality[38]. Photoluminescence (PL) - a technique which reveals the optical transitions in

a material - taken of samples with differing miscut, revealed no significant signal for the 6 degree samples. The technique of PL will be qualitatively discussed further in the following chapters, and PL data of the sample set used will be reviewed. The effect of miscut and the reasons behind worsening QD formation in the 6 degree samples will then be further investigated with another optical technique, photoreflectance (PR) and an electrical technique to identify particular material defects, deep level transient spectroscopy (DLTS).

1.4 Test Samples

Epitaxially grown n-type materials were fabricated in a 3 x 2" Veeco D125LDM metal organic vapor-phase epitaxy (MOVPE) reactor (exactly the same as the MOCVD process) at NASA Glenn Research Center in Cleveland, Ohio. Precursors of trimethylgallium (TMGa), trimethylindium (TMIn), and arsine (AsH3) were used for alkyl (column *III*) and hydride (column *V*) sources, respectively. Si_2H_6 flows with the gas as an n-type dopant in the grown material. A baseline set of samples was developed as a control using 2*K*, 6*K*, and 6*N* GaAs substrate miscuts. The baseline samples consist of a GaAs substrate (from Sumitomo Electric, specifications as outlined in the previous section) with a 500 nm layer of n^+-type Silicon doping of $2.4x10^{18}$ cm^3 followed by a 500 nm layer of *n*-type Silicon doping of $4.5x10^{16}$ cm^3 grown at 685℃.

A set of QD samples using the same 2*K*, 6*K*, and 6*N* GaAs substrate miscuts were grown as follows: 685℃ growth of a 500 nm n^+-type GaAs (Si $2.4x10^{18}$ cm^3) base layer over the GaAs substrate, then a 1000 nm layer of n-type GaAs (Si $4.5x10^{16}$ cm^3); the intrinsic region is then grown: 33 nm of low doped GaAs (Si $2x10^{15}$ cm^3), followed by 2 ML of InAs where the growth temperature was ramped down to approximately 450℃

for QD formation, and approximately 40 nm of low doped GaAs following; the temperature was brought back up to 685℃ for a final 4 00 nm layer of *n*-type GaAs. Due to material deposition differences in the growth chamber, the QDs tend to form in higher densities on specific parts of the sample wafer, which will be discussed further in the experimental sections of this report. Figure 7 provides a graphical depiction of the final baseline and QD samples produced. This specific layer structure was chosen in consideration of the DLTS study, due to requirements of depletion region width, W_D for measurement purposes, as will be discussed in detail later.

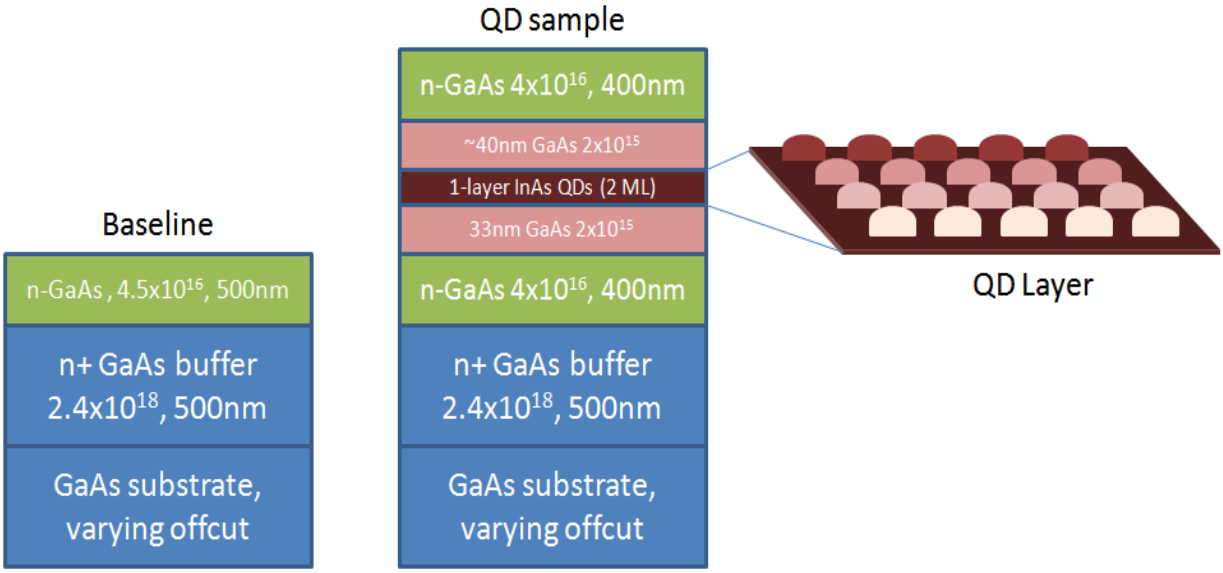

Figure 7: Sc stack of testing samples, showing the baseline configuration and the 1-layer (1x) QD sample. The lightly doped (considered effectively intrinsic) region of GaAs surrounds the QDs, the rest of the stack is composed of Silicon doped *n* or n^+-type GaAs.

Thus a total of six samples were grown, one baseline and one QD sample for each of the 2*K*, 6*K*, and 6*N* miscuts. A full sample wafer is shown below in Figure 7, where the sample was halved in order to accommodate both the optical spectroscopy and the defect analysis. For the DLTS study, the samples have about 600 nm of Ge/Au/Ni/Au acting as a back ohmic contact and 500 nm Au contacts were used to create Schottky diodes on the surface of the samples. The diodes are circular and

range from 100 μm to 600 μm in diameter. For PL and PR measurements, the samples were left as-grown. The samples will be further discussed in the following chapters as the sample characteristics pertain to the testing method used.

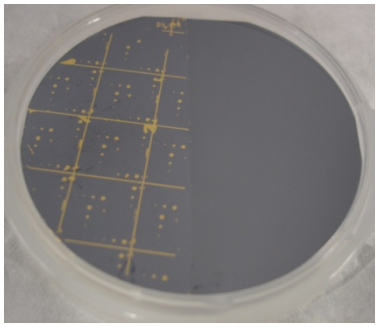

Figure 8: Top-down view of a sample wafer, halved where the left half is fabricated with Schottky diodes on the surface for DLTS testing and the right half is left as-grown for optical analysis.

1.5 Organization of This Work

The following chapters introduce the theoretical testing methods as they are utilized to characterize the sample set. The optical methods presented act as a complementary analysis to defect analysis, where optical energetic transitions and thus the band structure of the semiconductor may be explored as opposed to the activation energies and definitive properties of any existing localized or extended defects, respectively.

Chapter 2 delves deeper into the optical characterization methods of photoluminescence (PL) and photoreflectance (PR). The theory behind the PR spectroscopic technique is developed analytically, and the assumptions behind actual data treatment are presented. The experimental set-up, procedure and operation are discussed in detail. Finally data results are presented and evaluated.

In regards to the second characterization method of deep level transient spectroscopy (DLTS), Chapter 3 follows the same format as the previous chapter.

Chapter 4 presents discussion of the data obtained, including a comparison to published results of similar studies. Conclusions based on the preceding analysis are presented as well.

Chapter 2

Optical Spectroscopy

The interaction of carriers and photonic energy resulting in semiconductor band transitions, via single band gap material or material with many interband transitions, are an important metric when discussing semiconductor devices. The particular behavior of the incoming/outgoing photonic energy as related to carrier transitions within the material determine the capabilities of any device made with this semiconductor, be it for photovoltaic conversion, image detection, light emission, *etc*[52].

As mentioned previously, QDs can change the band gap of a material, and ordered QD arrays may realize the concept of the IBSC[23]. By observing the exact photonic energies absorbed or emitted by a QD semiconductor, the impact of QDs on material band transitions can be partially scrutinized and material optimizations toward the realization of a high-performance QD optoelectronic devices may be catalogued.

The spectroscopic methods mentioned in the introduction serve to identify the multiple band gaps present in QD material, which correspond to the QD size distribution, uniformity and density. Optical spectroscopy is of special interest in this study, as the method of optical probing is contactless and does not require device fabrication[53]. Thus the semiconductor material properties can be observed previous to any processing.

2.1 Photoluminesence (PL) Qualitative Theory

The optical spectroscopic method chosen in this study differs from PL, as will be explained in detail shortly. A qualitative understanding of PL is useful, however, as part

of the background for optical spectroscopy methods in general and in comparison to the method described in this thesis. PL is an optical probing method widely used for its ease of implementation[53]. The method concept is developed by first considering injecting a material with a high density of photons with energy higher than the material band gap, *i.e.* illuminating the sample with a focused laser beam. As illustrated in transition (a) of Figure 9, electron hole pairs (EHP) are created in the material, as electrons are energetically excited above the conduction band. As the carriers relax, seen in transition (b) of Figure 9, some of the energy is released thermally, and once reaching a state in the conduction band of the material the electron recombines and emits a photon at the transition wavelength. The emitted photons disperse from the probe area of the sample in a Lambertian pattern, hence a detector is placed perpendicular to the sample to collect the maximum amount of emitted light, as pictured in (c) of Figure 9. The measured peak emission photonic energies correspond very closely to the band gaps present in the material, where near the band edges the energy, *hv* of the emitted photon is given by the joint dispersion relation below,

$$\boldsymbol{hv = E_g + \frac{\hbar^2 k^2}{2m_r^*}} \qquad \textbf{Equation 3}$$

where E_g is the energy gap of the material, *k* is the Boltzmann's constant, and m_r^* is he reduced effective mass, combing both carrier effective masses[54]. Spontaneous emission rate, *I* is dependent on this emitted photon energy as,

$$\boldsymbol{I(E = hv) \propto \sqrt{E - E_g}\exp\left(-\frac{E}{kT}\right)} \qquad \textbf{Equation 4}$$

where *T* is the temperature, $\sqrt{E - E_g}$ is related to the joint density of states, and $\exp\left(-\frac{E}{kT}\right)$ to the distribution of carriers according to Boltzmann statistics. Plotting this

function of intensity versus energy, *hv* it is found that the peak of the PL spectrum is offset by $E_g + \frac{kT}{2}$, where $\frac{kT}{2}$ at room temperature is about 0.01 eV. This correction is omitted in the following analysis due to the incorporation of other instrumental error. Also, the intensity of the emitted photons increases with carrier generation produced by the power of the laser source.

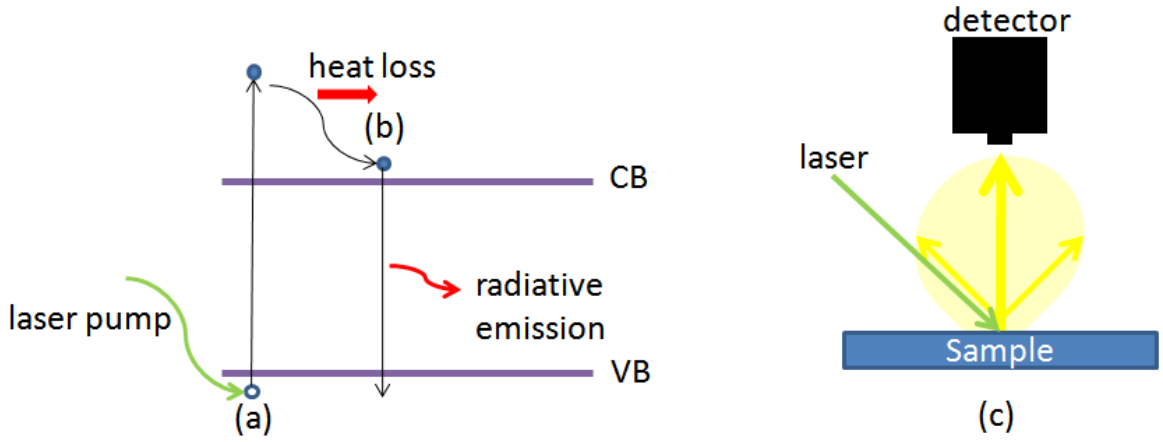

Figure 9: A laser pumps a sc sample, creating an EHP in the valence band (VB) as in (a), the electron is promoted above the conduction band (CB) and then loses energy due to thermalization and radiative emission as in (b). The emitted light radiates off the sample in a Lambertian pattern and a photodetector measures the intensity of emitted photons versus wavelength as in (c).

For quantum confined material such as QDs, this method can be useful in determining the interband transitions, where the emission from the occupied discrete states within the QD occurs by state filling from diffusion of excited carriers in the GaAs CB to the QDs (before radiative recombination to the VB)[7]. An intense luminescence signal from confined structures is typically observed due to the state filling from diffusion, but only if 1) the relaxation mechanism from bulk states to confined states is faster than radiative recombination from the bulk states to the VB, and 2) if there are only a few eigenstates for each QD energy sublevel. Either of these mechanisms may

be disrupted if the QDs are of insufficient dimensions. The Gaussian or Lorentzian-type emission spectra are fitted with distributional curves of that form, these distributional forms being a function of the apportionment of QD shapes across the wafer, and thus the discrete energy levels associated with varying dot size. Numerical analysis has shown a statistically favorable QD size appears after growth with less-favorable sizes distributed in a bell-shape [55], as seen in Figure 10 below, where the peak intensity of the curve indicates the highest transitional probability and thus the probable energy state of the most prominent QD, called the QD ground state. When attempting to observe multiple emission peaks such as WL and lower order QD transitions, however, the character of the Gaussian curves may be difficult to resolve; as the peaks become more convolved, the higher intensity emissions can drown out the signal of other transitions[56].

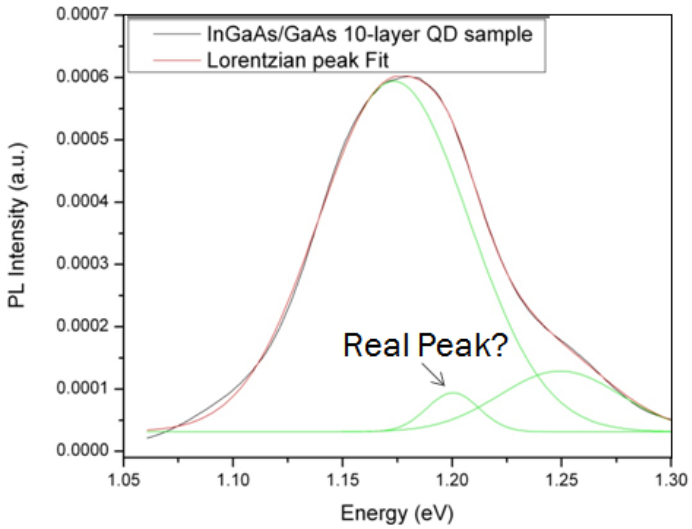

Figure 10: Photoluminescence for a 10-layer InAs/GaAs QD sample. The QD peak is fitted with multiple Lorentzian distributional forms shown in green, the sum of which is represented by the red fit line; however, it is difficult to conclude that the smallest peak is an actual QD transition energy, rather than an artifact of the fit.

For complete material characterization, and to efficiently observe the effects of changing material parameters on QD growth, it is necessary to resolve even the weakest interband transitions, as this relates to QD formation in terms of size, uniformity, and density. One may qualitatively consider a method that relies on a zero-crossing to identify a transition point, instead of a peak. This derivative measurement would essentially achieve better resolution of interband transitions, as peak emission intensity could be correlated directly to each zero-cross point. Thus PL is used in this study to verify and contrast data obtained by a more resolved derivative spectroscopy.

2.2 Photoreflectance (PR) Theory

PR is an optical modulation (derivative) spectroscopy method that characterizes semiconductor materials by observing a change in a material's dielectric function due to the variation of electric field[57]. The electric field in the sample is varied by an optical pump, usually a chopped laser signal. This modulation in the electric field changes the permittivity of the material and thus changes the reflectance of the sample and the intensity of the detected photons.

An optical detector collects both the modulated reflectance signal produced by the chopped laser and the constant reflectance signal produced by a probe light beam at a particular wavelength. The probe light, usually produced by a monochromator, is scanned over a range of wavelengths to produce the full PR spectra with measurements taken at specific intervals. This spectrum is related to $I(\lambda)\Delta R(\lambda)$ and $I(\lambda)R(\lambda)$ respectively; both terms are dependent on the wavelength, λ of the probe light, where $I(\lambda)$ is the intensity of the signal and $R(\lambda)$ is the reflectance component. Taking the ratio of these signals eliminates the intensity element and the normalized $\Delta R(\lambda)/R(\lambda)$

values plotted versus wavelength reveal the optical transitions present within the material.

To extract material band transitions from the derivative reflectance spectra, first the relation between reflectance and material dielectric function will be examined. Note that the dielectric function of a material, ϵ can be written as having both real and complex parts as below,

$$\epsilon = \epsilon_r + j\epsilon_i \qquad \textbf{Equation 5}$$

Knowing that the varying reflectance of the material, *R* is proportional to the dielectric constant, ϵ, and both are modulated by the incident laser signal, a general equation may be written as below,

$$\frac{\Delta \boldsymbol{R}}{\boldsymbol{R}} = \frac{\boldsymbol{1}}{\boldsymbol{R}}\frac{\boldsymbol{\partial R}}{\boldsymbol{\partial \epsilon_r}}\Delta\boldsymbol{\epsilon_r} + \frac{\boldsymbol{1}}{\boldsymbol{R}}\frac{\boldsymbol{\partial R}}{\boldsymbol{\partial \epsilon_i}}\Delta\boldsymbol{\epsilon_i} \qquad \textbf{Equation 6}$$

where $\Delta\epsilon_r$ and $\Delta\epsilon_i$ represent changes in the complex dielectric function due to laser modulation and the relation $\frac{\partial R}{\partial \epsilon_r}$ and $\frac{\partial R}{\partial \epsilon_i}$ are yet unknown. The relation between $\Delta R/R$ and the material's dielectric function can also be written as below,

$$\frac{\Delta R}{R} = \alpha(\epsilon_r, \epsilon_i)\Delta\epsilon_r + \beta(\epsilon_r, \epsilon_i)\Delta\epsilon_i \qquad \textbf{Equation 7}$$

where α and β are Seraphin coefficients[58] related to the unperturbed dielectric function, $\Delta\boldsymbol{\epsilon}_r$ and $\Delta\boldsymbol{\epsilon}_i$ are the changes in the real and complex dielectric function, respectively, due to modulation[57]. The Seraphin coefficients are fractional optical constants, functions of photon energy that have been experimentally determined for different materials and change dependent on observed spectral region, as seen in Figure 11.

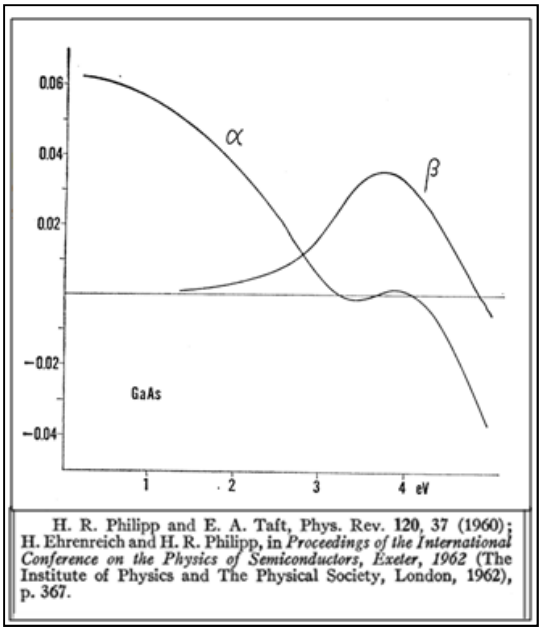

Figure 11: Seraphin coefficients, *a* and *b* for GaAs changing dependent on incident energy added to the semicondctor[58].

For the energy range studied for QD transitions, below 2 eV, the first coefficient, α dominates as seen in Figure 11 above and thus the imaginary part of Equation 7 is neglected. This is also referred to as the low field regime of reflectance spectroscopy[57], and the region where the fundamental band edge of the material exists[58]. This low-field case is defined by the electro-optic energy given by $\hbar\Theta$ being smaller than the spectrum broadening parameter, Γ. The energy $\hbar\Theta$ can be written as,

$$(\hbar\Theta)^3 = \frac{q^2\hbar^2\varepsilon^2}{2\mu_{II}} \qquad \textbf{Equation 8}$$

where q is Coulombic charge, ε is the electric field, and μ_{II} is the reduced interband effective mass accelerated in the direction of the uniform field.

The evaluation for the low field regime involves consideration of perturbation theory in its third derivative form for a good approximation to interband transitions[59]. Perturbation theory recognizes two related energies: that characteristic to the perturbation and that characteristic to the energy of the system. These relate

respectively to the potential change in the material, $q\varepsilon a_0$ (where the electric field, $\boldsymbol{\varepsilon}$ is not lattice-periodic and thus is directionally dependent with constant a_0) and to the energy separation being considered, E_g[59]. According to perturbation theory Equation 8 above may be written as,

$$(\hbar\Theta/\Gamma)^3 = \frac{q^2\hbar^2\varepsilon^2}{2\mu_{II}\Gamma^3} = \frac{q^2(\varepsilon\cdot\nabla_{\boldsymbol{k}})^2 E_g(\boldsymbol{k})}{8} \qquad \textbf{Equation 9}$$

where $\boldsymbol{k}$ is a wavevector; notice the introduction of the broadening term, Γ.

The change in dielectric function of a material, $\Delta\epsilon$ is related to the electric field, ε and the third derivative approximation of the unperturbed dielectric function, $X(\Gamma, E)$ as[59],

$$\Delta\epsilon(\varepsilon, \Gamma, E) \propto \varepsilon^2 X(\Gamma, E(\boldsymbol{k})) \qquad \textbf{Equation 10}$$

where $X(\Gamma,E)$ is defined as the linear optical susceptibility coefficient, and E is the probe wavelength.

The relation between the broadening parameter, Γ and the wavevector, $\boldsymbol{k}$ as seen in Equation 9 can be exploited in combination with Equation 10 to find the dielectric function, $\epsilon(\Gamma,E)$ of a material as[60],

$$\epsilon \propto Re[(E - E_g + i\Gamma)^{-m}] \qquad \textbf{Equation 11}$$

where E_g is the unknown material band gap, Γ is the spread or width of the lineshape and used as a fitting parameter, and m is a lineshape factor which changes dependent on the material band gap being investigated, be it a bulk band gap or interband QD transitions[57]. Again, only the real part of the dielectric function is considered for the low to intermediate field regimes due to the weighting of Seraphin coefficient α. If the state transition exhibits Lorentzian or Gaussian type dispersion (as in the case of QDs), the

value of *m* is equal to two[59]. This yields the final form of the relation between differential reflectance and material band gap as,

$$\frac{\Delta R}{R} = Re[C_1 e^{i\vartheta}\left(E - E_g + i\Gamma\right)^{-2}] \qquad \textbf{Equation 12}$$

where C_1 is a constant relating to the magnitude or intensity of the PR signal, and θ is a phase angle.

2.3 Experimental

In this section, both PL and PR data are presented. PL data is used to verify the energy transition values obtained from PR and to illustrate the differences between miscut samples as observed previously by Hubbard *et al*. To reiterate from section 1.3, in the nomenclature used here, 2*K* (6*K*) means 2 (or 6) degrees off the (100) lattice toward the [110] plane. 6*N* means 6 degrees off the (100) toward [111]. Six samples were grown for testing, three baseline samples and three QD samples with 2*K*, 6*K*, and 6*N* miscuts. The sample stack is pictured in Figure 7. Each sample was cleaved in half, and one side was left as-grown (no surface or backside metallization) for optical testing.

2.3.1 PL set up

A Spectra-Physics Argon-ion laser at 514.5 nm with adjustable power up to 130 mW is used as the excitation source for optical probing of the samples. The laser signal is physically modulated by a mechanical chopper at a frequency of 377 Hz. A 780 nm cut-on filter is placed in front of the IHR 320 Monochromator to filter out any spurious laser signal. The PL signal is focused into a 2 mm slit of a selective-wavelength IHR 320 Monochromator (with 3 gratings at 330 nm, 750 nm, and 1500 nm blazes, respectively),

which greatly reduces any background distortion, and feeds the low-noise signal through a 2 mm exit slit to a thermoelectrically cooled Ge photodiode. The A.C. signal from the detector is measured by an SRS 830 lock-in amplifier, which phase-locks to the chopped signal. The PL is setup is shown below,

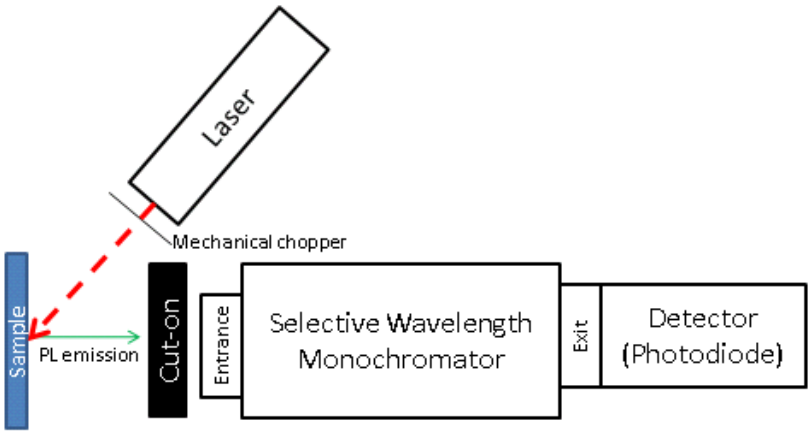

Figure 12: PL set up for optical probing of the sample.

The PL spectra obtained for all the QD samples are shown below. PL was taken for the baseline samples as well (not pictured) and each sample revealed a GaAs band edge transition of 873 nm or 1.42 eV. As examined previously, the PL signal from the 6 degree miscut QD samples is much weaker than in the 2 degree sample. The QD signal can be observed between 1.0 eV and 1.3 eV and the WL between 1.3 eV and 1.4 eV.

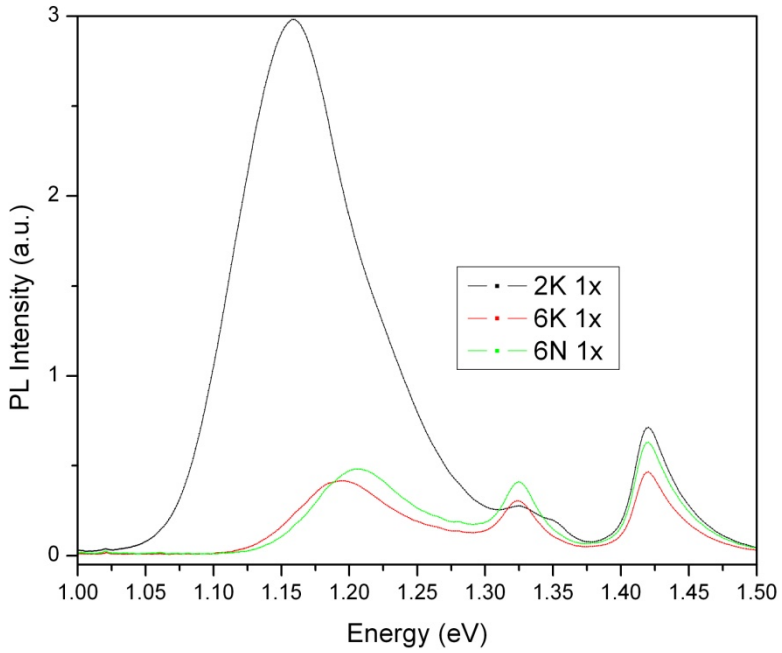

Figure 13: PL spectra taken for the QD samples. The QD signals of the 6 degree miscut is very poor compared to the 2 degree sample.

The degradation in signal intensity seen in the 6 degree samples could be attributed to a decrease in radiative recombination, and corresponding increase in non-radiative recombination. It is generally found that large PL signals correlate with good interface properties[61]. Nevertheless, PL degradation may not be due to an increase in extended defects above the QD layer, as Lobo *et al.* observed strong radiative emission from QDs, even after formation of a dislocation array[51]. Other studies suggest that a sharp drop in luminescence intensity from InAs/GaAs QDs is associated with increasing density of incoherent (lacking disc or pyramidal structure) InAs islands, citing these incoherencies as being optically inactive[62]. This argument could be supported by the above PL data, where the WL signal for the 6 degree samples is more intense than that of the 2 degree, indicating poor QD formation where the optically active QDs are less dense in this material. The suggestion of an increase in non-radiative recombination in

the 6 degree samples as related to defect generation will be further explored in the DLTS section of this report. A shift in QD peak versus transition energy is observed in the PL spectra from sample to sample, as tabulated below. These peak values were found using a Gaussian fit to the observed QD peaks, and error values result from the quality of convergence of the fit.

Table 1: Gaussian fits were used to extract these peak values which correspond to energetic transitions within the QD and WL.

Sample	WL (eV)	Error (meV)	QD1 (eV)	Error (meV)	QD2 (eV)	Error (meV)
2K 1x	1.32	0.3	1.1578	0.1	1.2425	0.6
6K 1x	1.32	0.2	1.2109	0.3	-	-
6N 1x	1.32	0.2	1.2241	7.3	-	-

Note that only the 2*K* sample resolved a second Gaussian peak, indicating a different QD transition and thus a greater concentration of QDs with this transition energy than in the 6 degree samples. The shift in energy between the 6 degree QD samples and the 2 degree sample is about +50 meV or a 5% change. This is indicative of changing QD size, where the higher transition energy would suggest a QD level closer to the conduction band, or a smaller QD.

2.3.2 PR Set up

The experimental setup for PR measurements is shown in Figure 14. Light from an Optronics Laboratories OL750 Monochromator is reflected off the sample, as well as the modulated optical signal produced by a Spectra-Physics Argon-ion laser at 514.5nm with adjustable power up to 130 mW. The laser signal is physically modulated by a mechanical chopper at a frequency of 377 Hz.

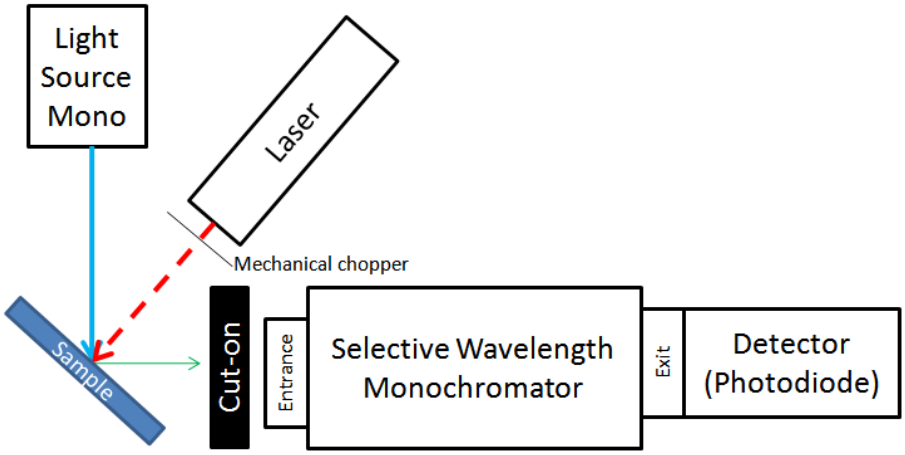

Figure 14: PR set-up.

Both the A.C. modulated signal and the D.C. signal are collimated by an 8 cm focal length lens and focused by a 150 cm focal length lens. A 780 nm cut-on filter is placed in front of the IHR 320 Monochromator to filter out any spurious laser signal. The signal is focused into a 2 mm slit of a selective-wavelength IHR 320 Monochromator (with 3 gratings at 330 nm, 750 nm, and 1500 nm blazes, respectively), which greatly reduces any background distortion, and feeds the low-noise signal through a 2 mm exit slit to a thermoelectrically cooled Ge photodiode.

The A.C. signal from the detector (proportional to $I(\lambda)\Delta R(\lambda)$ where $I(\lambda)$ is the signal intensity at a specific wavelength) is measured by an SRS 830 lock-in amplifier, as pictured in Figure 15. The D.C. signal from the detector, or $I(\lambda)R(\lambda)$, is measured by a Keithley 2400 Digital Multimeter. A LabView computer program coordinates the wavelength scan for each measurement, and reads the two signals which are then normalized to $\Delta R(\lambda)/R(\lambda)$ to eliminate the intensity factor and generate the PR spectra plot over versus wavelength, as shown in Figure 15. Typically $I(\lambda)\Delta R(\lambda)$ is 10^{-4} to 10^{-6} of $I(\lambda)R(\lambda)$[57].

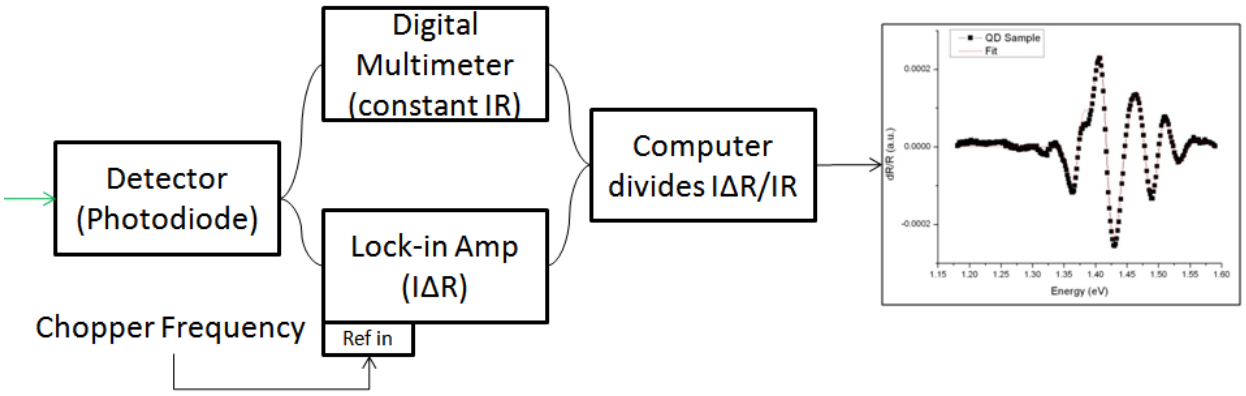

Figure 15: PR signal detection and interpretation. Computer outputs graphical PR spectra.

2.3.3 PR Testing Results

Error for all measurements was based on error characterized in the test set-up and was found to vary for each data point taken, where modulations in the AC signal closer to zero experienced greater error due to the detector noise floor of ~$1x10^{-7}$. Error from the respective fits of each signal is given in tabular form for each data set. For the following data, the average error for the evaluated signal was about 5%, and any data that experienced measurement error of 10% or above was not treated.

Outside of the main sample set presented in the introduction, several other QD samples were tested to explore the utility of the PR testing method and verify functionality of the system. First, an identification of the QD and WL signals was performed, both by comparative study of previously reported transition energies in InAs/GaAs QD materials and by visual inspection of the PR signal. The differences in the PR signal, as seen in Figure 16 can be attributed to differences in confinement, where the WL acts as an effective QW and thus exhibits different changes in reflectance. The QD and WL transitions are fit according to the third derivative

functional form of Aspnes from Equation 12. Typical wetting layer energies have been shown to be present just below the GaAs material band gap of 1.42 eV and extend to values of approximately 1.3 eV, and QD signals can be shown to be below ~1.3 eV[64].

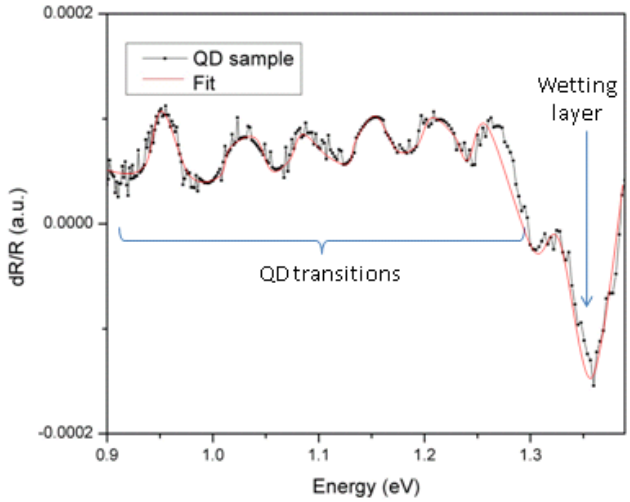

Figure 16: PR spectra highlighting the differences in signal between QD and wetting layer transitions.

The PR signal in Figure 16 was collected from a 10-layer QD sample, where multiple InAs QD layers have been deposited in sequence, separated by a GaAs buffer layer. Details of this growth can be found elsewhere[38]. Table 2 below shows the comparative study of the extracted QD transitions from this 10 layer QD sample and other PR studies from Rowland *et. al*[64] of a 2-layer sample and from Pollak *et. al*[57] 1-layer samples. Percent error is shown between the measured values and those reported in literature.

Table 2: 10 layer QD stacked structure energetic transition values extracted from PR compared with other transitions experimentally observed in literature.

Transition	10 layers	+/-	Rowland[64] 2 layers	%Error	Pollak[57] 1 layer	%Error
	Energy (eV)	(meV)				
QD1	0.960	0.1	1.053	9%	-	-
QD2	1.059	0.1	1.105	4%	-	-
QD3	1.122	0.2	1.160	3%	1.140	2%
QD4	1.173	0.1	1.224	4%	1.219	4%
QD5	1.240	0.2	1.277	3%	1.260	2%
WL1	1.300	6.3	1.365	5%	1.373	5%

Note that the lowest QD transition energy shifts from 1.14 eV, with one layer of QD structure, to 0.96 eV with 10 layers, and that only three QD signals in the 1 layer material have been resolved. Also a shift to lower energies of about -50 meV is observed in general from 2 layers to 10 layers. This could suggest that increasing QD layers may have an effect on QD size, uniformity, and density. With a shift towards lower QD energies with increasing number of layers, the addition/subtraction of layers could prove to be an effective QD engineering tool to control the exact properties of such a material. Stacks of 20, 40, and 60 layers of repeating QD structures have been grown, hence further investigation of these properties could conclusively confirm these trends.

From the theoretical discussion previous, a low-field assumption was the basis for the development of the TDFF; however, if the low-field criterion is not satisfied the dielectric function can exhibit Franz-Keldysh oscillations (FKOs)[57], as shown in Figure 17. In this case, oscillations in the reflectance signal are observed resulting from the bulk (GaAs) bandedge transition, *i.e.*, beginning at energies around 1.42 eV and continuing to higher energies. The subsequent x-axis crossings (labeled E_n in Figure

17) are no longer indicative of an energy transition within the material. The period of these FKOs is determined by the value of the dominant electric field in the structure. The sample used for the FKO analysis was a simple n-type GaAs baseline sample on a 2*K* miscut GaAs substrate.

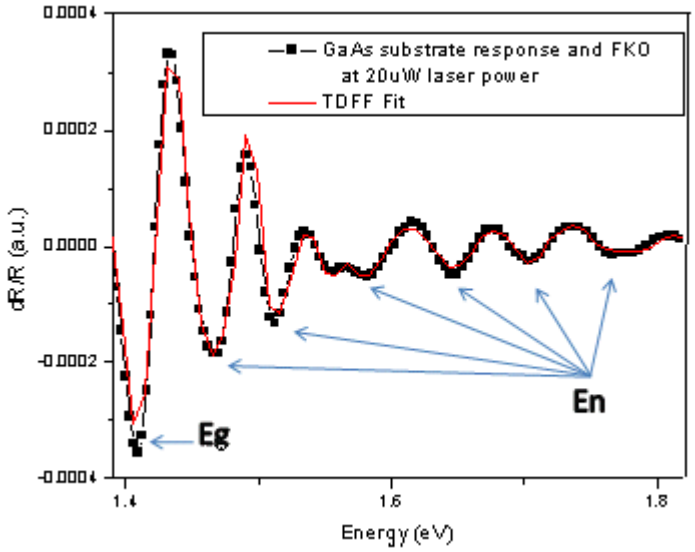

Figure 17: FKOs observed for a GaAs sample.

The energy values extracted by the TDFF fit of the GaAs bandgap, E_g and FKO extremum, E_n can be plotted versus an index number 'n', this gives a linear trend, the slope of which is $(\hbar\theta)^{3/2}$ as below[57],

$$n\pi = \left(\frac{4}{3}\right)[(E_n + E_g)/\hbar\theta]^{3/2} \qquad \textbf{Equation 13}$$

where *n* is an integer value used as an index number for each extremum E_n. The linear plot of these FKO transition values is show in Figure 18 below,

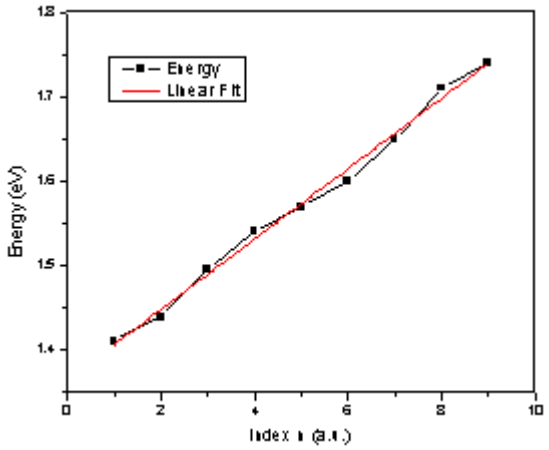

Figure 18: Linear fit to the extracted transition energy of the FKO PR data versus index number *n*.

The slope, $(\hbar\theta)^{3/2}$ of this fit may be used as below to extract the electric field (*F*) within the material,

$$(\hbar\theta)^3 = q^2\hbar^2F^2/2\mu_{||} \qquad \textbf{Equation 14}$$

where $\mu_{||}$ is the reduced interband mass. The value for the electric field in this sample obtained from using FKO analysis was found to be 120 kV/cm (with a standard fitting error of +/- 2.5 kV/cm). A theoretical calculation of the field expected in this sample was determined as below,

$$|F| = \frac{qN_DW_d}{\epsilon_s} \qquad \textbf{Equation 15}$$

and the field from this ideal equation was calculated to be 64.8 kV/cm, about half the extracted value. This method thus could be an accurate method for finding material electric fields, a parameter which is very important as related to carrier transportation in the semiconductor material. When investigating QD samples, FKO may indicate changing fields dependent on the QD region, a possibility for the continuation of this PR work.

2.3.4 PR and Miscut Results

All the bandedge transitions observed in the PR data corresponded exactly to the PL data values of 873 nm or 1.42 eV (with an error of 2 meV), as shown in Figure 19. Only the 2*K* sample showed enough modulation in reflectance in the QD/WL region to resolve a distinct PR signal, as shown in Figure 20. The QD transitions which can be fit according to the third derivative functional form of Aspnes from Equation 12 (in green in Figure 20) are labeled as QD1, QD2, QD3, and QD4 below. One transition is characterized as starting with a positive peak and then reaching an inflection point (where the energy state value is measured) and a subsequent negative peak in the signal. These transitions were found by evaluating the error (which was high below about 980 nm); any transition with error values less than or equal to 5% was defined as a QD state. Above 1100 nm, no change in reflectance signal was observed, indicating that QD1 is the ground state (or lowest QD transition) of the material. The resolved transitions are shown in Table 3, where the WL signal (not shown in Figure 20) was fit independently of the QD signals.

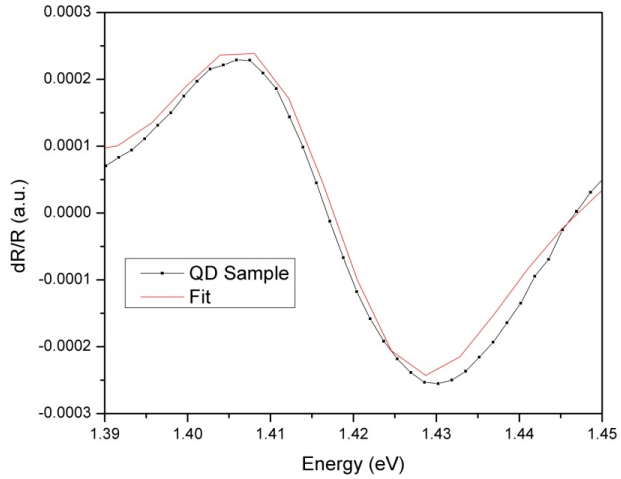

Figure 19: PR data for the GaAs bandedge of a QD sample. All baseline and QD samples showed a GaAs transition at 1.42 V.

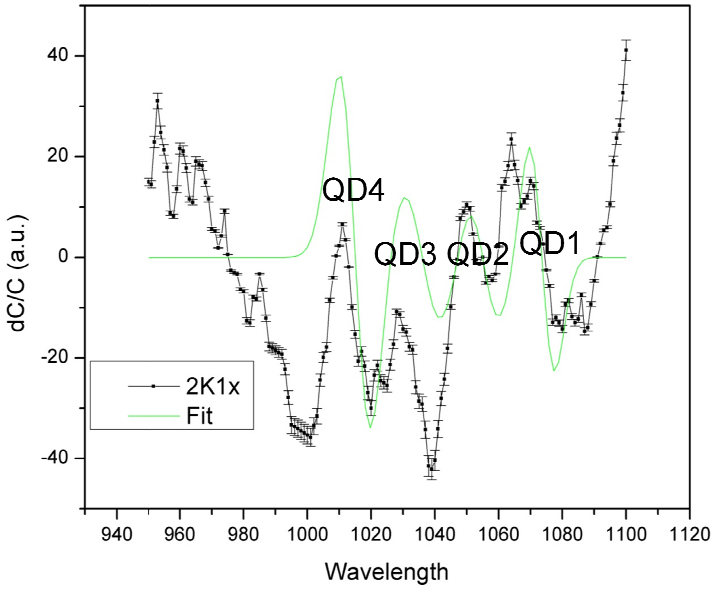

Figure 20: PR signal obtained in the QD region for the 2*K* sample.

Table 3: Extracted QD transition energies for the 2*K* samples.

Sample	WL (eV)	+/- (meV)	QD1 (eV)	+/- (meV)	QD2 (eV)	+/- (meV)	QD3 (eV)	+/- (meV)	QD4 (eV)	+/- (meV)
2K 1x	1.34	2	1.16	2	1.18	60	1.20	110	1.22	204

The resolution of two lower-order QD transitions of 1.20 eV and 1.22 eV are not as accurate due to fitting error, but would represent a distribution of QD sizes. Also, the transition of 1.20 eV or 1.22 eV could be correlated to the ground state transitions seen in the PL of the 6 degree samples, and could indicate that growth related to the 6 degree miscut inhibited formation of QDs to an extent. The PR data collected for the 2*K* sample corresponds nicely to PL data, where the ground state transitions resolved from both methods varies by only 0.1%, and is found to be about 1.16 eV. The PR signal for this sample, however, could be better resolved with an optimized set-up, as will be the goal of future work in this area.

2.3.5 Optical Spectroscopy Miscut Discussion

The results obtained from optical examination of the material confirm those previously obtained by Hubbard *et al.*[38] where the 2 degree miscut samples showed notably stronger PL signal for the QDs than the 6 degree sample, thus indicating a decrease in radiative recombination within the QD region. Also the 6 degree samples showed a shift in QD transition energy of +50 meV, where the 6 degree QD transitions occurred at a higher energy than the 2 degree sample. This would suggest a diminishing QD size from 2 to 6 degree miscut substrate, where the 6 degree miscut substrates develop QDs with higher transition levels (*i.e.*, the QD confined energy state is closer to the CB).

PR results obtained show WL and QD energetic transitions similar to those observed in PL for the 2 degree sample. Also, the energetic transitions extracted for the WL and QD correspond well to those previously observed in literature[63,64] where the WL energetic transition values lay between 1.3 eV and 1.4 eV and the QD transitions appear between 1.0 eV and 1.3 eV. The ground state QD transition for the QD sample was found to be at 1.16 eV. Several lower-order transitions, correlating to QD energetic transitions of 1.18 eV, 1.20 eV and 1.22 eV were observed as well, better revealing the QD size distribution within the sample.

PR signal for the 6 degree miscut samples were not resolved, thus the change in reflectance, ΔR signal for this material is not strong. The ΔR signal corresponds to the A.C. output of the detector, as discussed in Chapter 2. The limit of this detector is ~1.6×10^{-7}, and thus the incremental changes in ΔR may have been below this threshold.

Chapter 3

Deep Levels and Deep Level Transient Spectroscopy (DLTS)

3.1 Deep Levels and Effects on Device Performance

Deep levels are typically defined as those energy states that exist within the middle third of the material band gap, as shown in Figure 21. However a more rigorous definition describes deep levels as having highly localized wave functions[65]. Compared with shallow defects that can be approximated with an effective hydrogen model, deep levels are characterized by very high binding energies that interact strongly with the crystal lattice and can trap a significant amount of carriers. Also, Fermi level pinning may occur due to deep level behavior[65]. This pinning leads to band bending and the creation of carrier barricades or traps. The activation energy, capture cross section and concentration of these defects change with each material and processing factors.

Figure 21: Showing the energy band characteristics of deep levels versus shallow impurities, where deep levels typically reside in the middle third of the band gap.

The deep levels in *III-V* materials are usually viewed as degrading overall device performance, such as decreasing carrier lifetime. For example, in GaAs-based devices it is postulated that common shallow donors combine with unknown defects, termed defect X, and form deep DX centers that are non-radiative[65]. Also, the arsenic anti-site

defect known as EL2, with activation energy between 0.80 eV and 0.85 eV[66] is a commonly cited GaAs deep level[65]. For a more complete list of common deep levels in GaAs, please refer to Appendix I.

The reduction in the effective carrier lifetime (τ) caused by these defects can cause a gain in recombination current (I_{re}) in solar cells as illustrated by Shockley-Read-Hall theory below[81],

$$\boldsymbol{I_{re} \propto \frac{1}{\tau} \exp\left(\frac{qV}{nkT}\right)} \qquad \textbf{Equation 16}$$

where V is the applied voltage and n is the ideality factor. This leads to lower cell efficiencies where increased recombination current lowers the current available for extraction[82], and the introduction of deep levels can also cause lower open-circuit voltages[67] and other negative device effects. In transistors, deep levels can cause a variety of degradation, including drain lag and current collapse[68].

As stated in the introduction, dependent on material composition ratio, lattice mismatch between GaAs and InAs is fairly minimal (around 7%)[69]. Following this, although QDs can now be fabricated with a high degree of lattice precision, defects causing non-radiative recombination and carrier trapping in the lattice structure of the QD device, such as dislocations and point defects, may still have a significant effect on the material performance[70,71]. Thus an effective method for probing these deep level defects and characterizing the trap parameters has much utility with regards to understanding device operation and possibly eliminating or compensating for degradation effects. Such defects have been probed using a variety of methods including low-energy positron beam measurements for defect depth profiling[72], photo-

induced current transient spectroscopy (PICTS)[73,74], and deep level transient spectroscopy (DLTS)[71,70]. Capacitance and admittance methods, where characterization of the material requires multiple measurements at different frequencies and temperatures[75], is also a well-known method of deep defect profiling. However these methods have limitations in flexibility[76].

In this study, DLTS is the preferred defect characterization technique, as the sensitivity of this method is specific to the space-charge region (SCR) of a junction. Thus the QD transition properties and QD-induced defects in proximity to this region can be effectively observed and highly resolved[79]. Also, DLTS reveals accurately the thermal activation energies, trap concentration, and cross-sectional dimensions of deep level defects, data which other defect characterization methods mentioned previously do not disclose completely[76,77]. This defect data corresponds to the Fermi level behavior of traps which may be caused by QD growth, and thus can produce metrics related directly to current density and voltage limiting behavior in QD semiconductors[78].

As mentioned, the growth of QDs in the i-region of a solar cell, *i.e.*, InAs/GaAs QDs, may introduce defects[78]. Dislocations, especially in the emitter region of the *p-i-n* solar cell, can degrade the performance of the cell overall and in some cases the resulting current degradation completely balances the current enhancement produced by the QDs[23]. Also, a lowered open-circuit voltage in QDSCs has been consistently observed[22,23]. For this reason it is important to investigate the defect levels associated with QD insertion, specifically deep levels which can significantly affect solar cell performance.

The sub-band gap behavior of QDs are theorized to trap and emit charge similar to processes of point and extended defects[79]. Hence, most studies of QD devices with DLTS to date have characterized the QD properties alone, such as sub-band levels and carrier emission from the QD states (which require sub-77K temperature scans due to the QD states being less prone to thermal emission effects). A study of DLTS QD transition states was not performed here, as the complementary optical methods of PL and PR are able to easily extract these discrete energy transition values within the QD at room temperature. The main concern of this study is the evolution of defects within the sample as related to QD growth. A DLTS study published in February of 2010 comprehensively shows such defect profiling in multi-layer GaAs(001)/InAs/InGaAs/GaAs QD samples[71]. The effect of the different QD growth optimization techniques used in this study on defects observed using DLTS may thus be compared with the DLTS data gathered by Asano *et al.* and others, further advancing the understanding of how deep level defects evolve within QD material.

3.2 Practical and Theoretical Discussion of DLTS

Lang introduced DLTS in 1974 as a spectroscopic method for characterizing deep level defects in semiconductors[77]. The original method is based on capacitance transients measured across a p^+/n junction diode. His system produced a plot of these capacitance transients versus temperature, *i.e.*, a transient spectrum, revealing a peak associated with each deep level or trap. Thus DLTS can be used to observe majority and minority carrier traps, especially those close to the Fermi level[77].

Here, a special case of a p^+/n junction will be considered for the development of DLTS theory. The sample is held at a certain reverse bias, V_R while a filling pulse

voltage, V_P varies the reverse bias seen by the diode and in turn varies the width, W_D of the depletion region in the p^+/n junction. The transient can qualitatively be understood as follows: during the positive pulse (V_P) the depletion region (W_D) shrinks as W_D is proportional to $\sqrt{(|V_R| - V_P)}$ and the junction capacitance (C) increases significantly as this is proportional to $1/W_D$. The testing method is illustrated below.

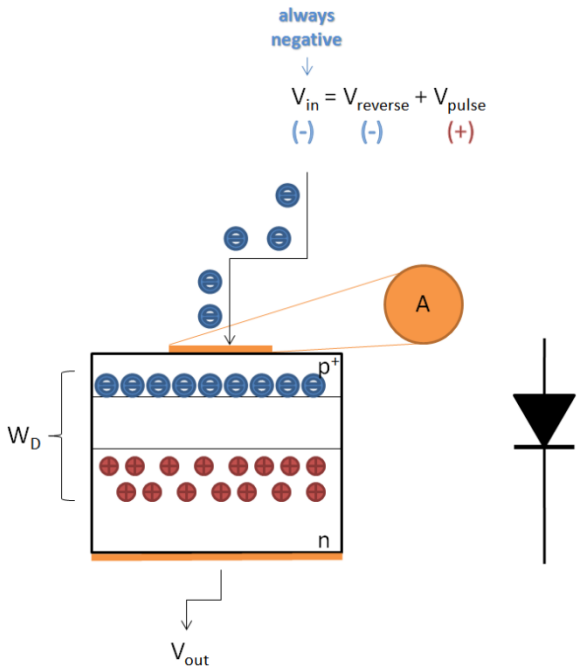

Figure 22: Illustration of the testing method for a p^+/n diode using DLTS, where W_D is the width of the depletion region, A is the area of the diode pad being probed.

Most notably, during the positive filling pulse, $+V_P$, the former depletion region is now swamped with electrons, which become quickly trapped by any donor-type deep levels (marked at an energy E_{Tn} in the energy band diagram in part (b) of Figure 23), as shown in parts (c) and (d) in Figure 23. Once the pulse is over and V_R is restored, the trapped electrons are now brought into the depletion region (shown in part (e) of Figure 23), lowering the *n*-side effective doping thus slightly expanding the depletion region further to that side of the junction, hence decreasing the observed capacitance. These

electrons are eventually thermally emitted back to the conduction band, shown in part (e) of Figure 23. This rate of emission is proportional to $e^{-e_n t}$ where e_n is the electron thermal emission coefficient. As the electrons leave the depletion region, W_D is returned to its original value at V_R and the capacitance follows a nearly exponential restoration to its previously constant value, $C(V_R)$. This change in capacitance, from its lowered value during the filling pulse to its static value at constant V_R, observed in a specific time interval defines the capacitance transient, $C(t)$.

The measured capacitance transient, $C(t)$ curve versus temperature is dependent on a time interval specified by the tester, called the transient window. Often DLTS is referred to as a rate window analysis, where the width of a measurement window, t_{window} is based on the beginning and end time of the measurement, t_1 and t_2 respectively, as pictured in Figure 24. Thus the change in capacitance $C(t)$ is found by taking the difference between the sampled values of $C(t_1)$ and $C(t_2)$. This capacitive change may become more rapid dependent on temperature, as thermally activated traps begin to capture more carriers and subsequently release them, as illustrated by the changing capacitance rate decay observed over temperature in Figure 24. At lower temperatures, the transient decays slowly such that the difference $C(t)$ is near-constant, and at high temperatures the signal reaches its quiescent value before the start of the transient window, t_1.

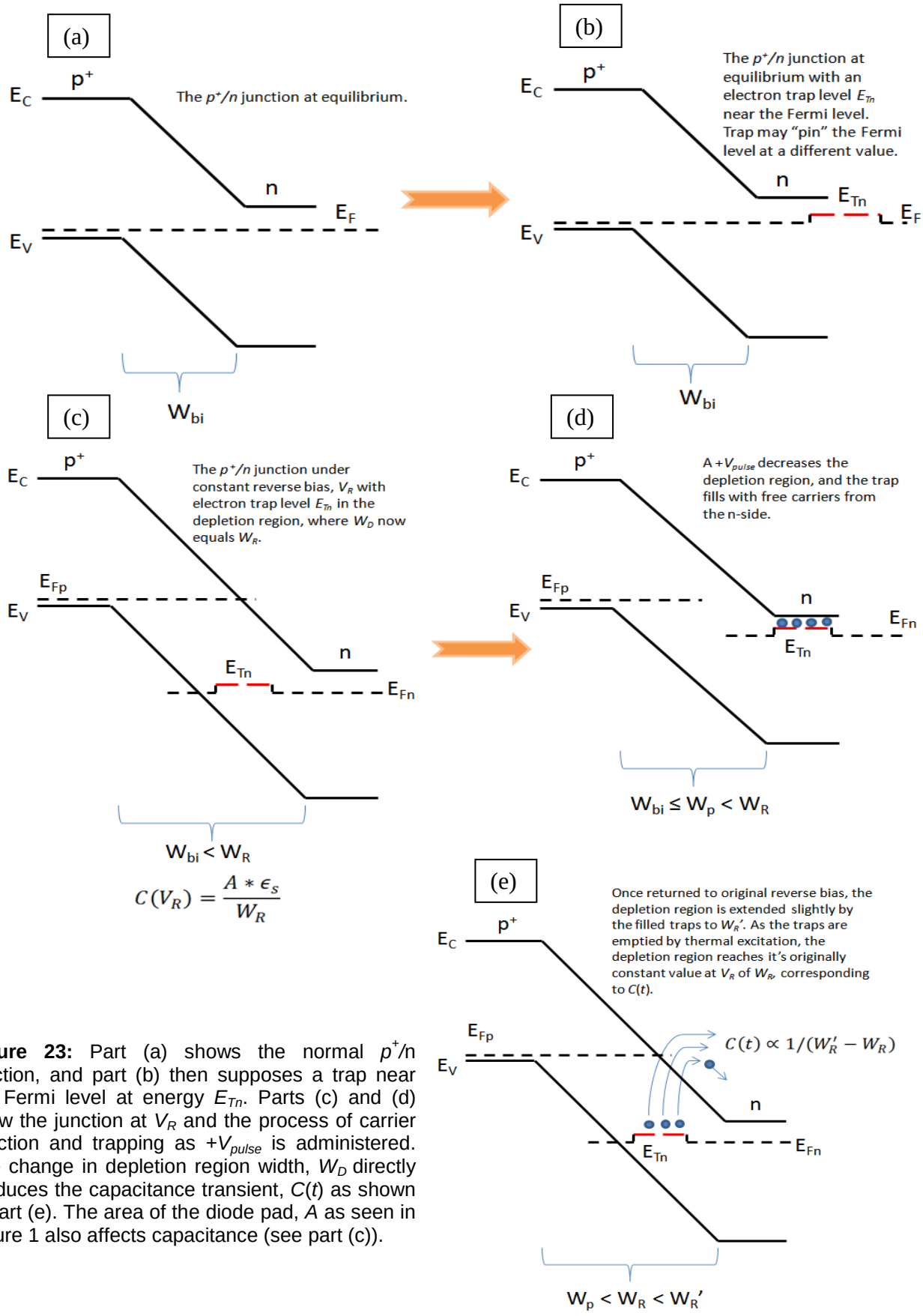

Figure 23: Part (a) shows the normal p^+/n junction, and part (b) then supposes a trap near the Fermi level at energy E_{Tn}. Parts (c) and (d) show the junction at V_R and the process of carrier injection and trapping as $+V_{pulse}$ is administered. The change in depletion region width, W_D directly produces the capacitance transient, $C(t)$ as shown in part (e). The area of the diode pad, A as seen in Figure 1 also affects capacitance (see part (c)).

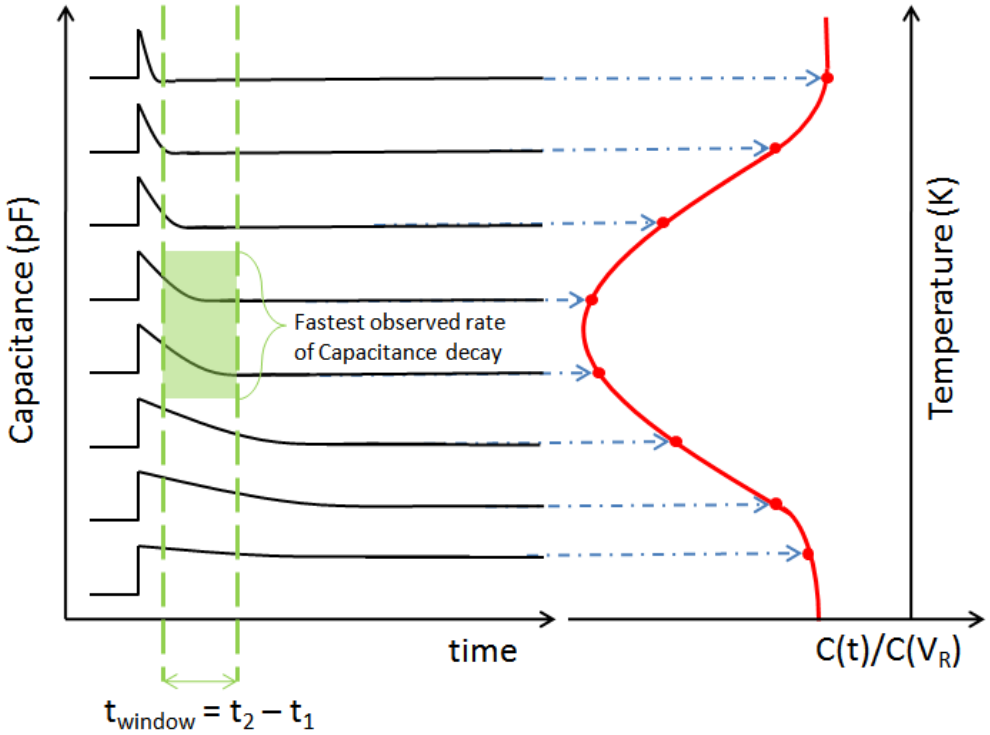

Figure 24: Sampled data points of $C(t) = C(t_2) - C(t_1)$ measured versus temperature which produce the DLTS spectra, pictured here as the red curve. $C(t)$ is normalized by the constant reverse bias capacitance, $C(V_R)$.

A peak in $C(t)$, monitored by the capacitance meter and normalized by the constant capacitance $C(V_R)$ of the sample, over temperature indicates an active trap and it would follow that trap parameters may be extracted from this transient. To fully describe this process quantitatively and relate trap concentration, capture cross section, and activation energy to the capacitance transient, the differential equation from Shockley Read Hall theory that describes electron occupancy of a trap may be examined as below,

$$\frac{dn_t}{dt} = c_n n p_t + e_p p_t - e_n n_t - c_p p n_t \qquad \textbf{Equation 17}$$

where n_t (p_t) is the concentration of filled (empty) electron traps in number per cm^3, c_n (c_p) is the electron (hole) capture coefficient in cm^3 per second, e_n (e_p) is the electron (hole) thermal emission coefficient in seconds^{-1}, and n (p) is the free electron (hole) concentration in number per cm^3. The processes of capture and emission from the trap level can be represented in the energy band diagram as below,

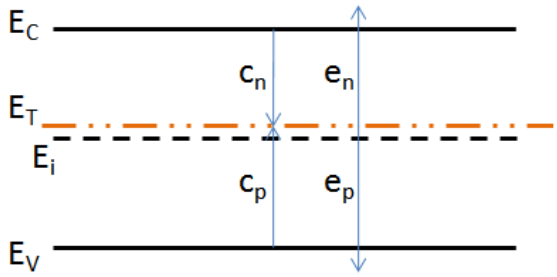

Figure 25: Band diagram illustrating the mechanisms of electron and hole capture (c_n and c_p) and emission (e_n and e_p) from a trap state.

Equation 17 can be simplified if we consider only electron traps in the n-type material, so p and e_p are neglected. Also in the depletion region, electron emission greatly dominates capture rates, hence $c_n n << e_n$ and Equation 17 can be re-written as below,

$$\frac{dn_t}{dt} = -e_n n_t \qquad \textbf{Equation 18}$$

for the time following the end of the pulse, $t > 0$ where V_P is applied when $t < 0$. If the initial condition is taken to be $n_t(0) = N_t'$, where N_t' is taken to be the active trap concentration at a given temperature, the solution to the above first-order differential equation is as below,

$$n_t = N_t' e^{-e_n t} \qquad \textbf{Equation 19}$$

The above equation describes the emission transient observed following a voltage pulse. The relation between this emission transient and junction capacitance follows rather simply, considering the charge density in the depletion region to be $\rho = qN_D'$ where N_D' is an effective donor concentration produced by $N_D - n_t(t)$. Using this N_D' in the typical relation for capacitance in a one-sided p^+/n junction, Equation 20 is obtained.

$$C(t) = \sqrt{\frac{q\epsilon_s}{2(V_{bi}+V_R)}} * \sqrt{N_D - n_t(t)} \qquad \textbf{Equation 20}$$

where V_{bi} is the junction built-in junction potential, and ϵ_s is the dielectric constant of the semiconductor material. This can be further simplified by multiplying the right hand side by $\sqrt{N_D}/\sqrt{N_D}$ where the constant background capacitance, $C(V_R)$ is as below,

$$C(V_R) = \sqrt{\frac{q\epsilon_s N_d}{2(V_{bi}+V_R)}} \qquad \textbf{Equation 21}$$

Hence Equation 21 can then be written as below,

$$C(t) = C(V_R) * \sqrt{\frac{N_D - n_t(t)}{N_D}}$$

$$= C(V_R) * \sqrt{1 - \frac{n_t(t)}{N_D}} \qquad \textbf{Equation 22}$$

Finally assuming $n_t(t)/N_D \ll 1$, the above can be approximated using the binomial expansion,

$$C(t) = C(V_R) * \left[1 - \frac{n_t(t)}{2N_D}\right] \qquad \textbf{Equation 23}$$

thus describing the capacitance transient in terms of deep level occupancy. Combining this with the result derived for trap emission in Equation 19, the final relation between trap concentration and the capacitance transient can be written as below,

$$C(t) = C(V_R) * \left[1 - \frac{N_t'}{2N_D} e^{-e_n t}\right] \qquad \textbf{Equation 24}$$

hence confirming that the capacitance transient follows an exponential form, and showing that the peak or magnitude of this transient has a dependence on trap concentration, N_t' and a time constant related to the thermal emission coefficient, e_n. Note that some traps or defects may not follow the dependence on emission through an exponential decay, for example isoelectronic traps.

Determining the rate coefficient, e_n which is constant for a specific set of experimental inputs defining the transient window, represented as $t_{window}=t_2 - t_1$ is a matter of observing the given capacitance values at time t_1 and t_2 as below,

$$C(t_2) - C(t_1) = C(V_R) * \frac{N_t'}{2N_D} [e^{-e_n t_1} - e^{-e_n t_2}] \qquad \textbf{Equation 25}$$

Differentiating this with respect to time in order to find the maximum decay rate at a specific temperature associated with a defined transient window, where the only time dependence on the right hand side is assumed in the exponential term, and equating the result to zero gives the maximum (or resonance vs. temp) of the thermal emission coefficient as,

$$e_n = \frac{\ln({}^{t_1}/_{t_2})}{t_1 - t_2} = \frac{\ln({}^{t_2}/_{t_1})}{t_2 - t_1} \qquad \textbf{Equation 26}$$

where, as mentioned previously, t_1 and t_2 define the transient window chosen by the operator. From the calculated rate coefficient, the trap concentration can be found as below, where all parameters on the right hand side are determined from experiment.

$$N_t = \frac{\frac{2N_D}{C(V_R)} * Max|C(t_2) - C(t_1)|}{[e^{-e_n t_1} - e^{-e_n t_2}]} \qquad \textbf{Equation 27}$$

where N_t is the evident total defect concentration, and $Max|C(t_2) - C(t_1)|$ is the magnitude of the DLTS spectrum at the peak emission temperature.

For the system used in this study, the defect concentration is given as below,

$$N_t(cm^{-3}) = \frac{6 * N_D * Max(|C(t)|)}{C(V_R)} \qquad \textbf{Equation 28}$$

where N_D is the dopant concentration, $Max(|C(t)|)$ is the maximum peak capacitance observed and $C(V_R)$ is the background capacitance entered or measured by the user. The constant numerical value is determined from the system constant of $t_2 = 5.3 * t_1$.

Upon further examination of this method, as the transient window widens or shrinks based on the user's input (*i.e.*, the change in capacitance, $C(t)$ is observed over a larger or smaller time interval) the $C(t)/C(V_R)$ peak observed over temperature shifts slightly, as seen in Figure 26, representative of multiple DLTS spectra. An example of multiple peak points taken from DLTS spectra plots of varying transient windows is shown in Figure 27.

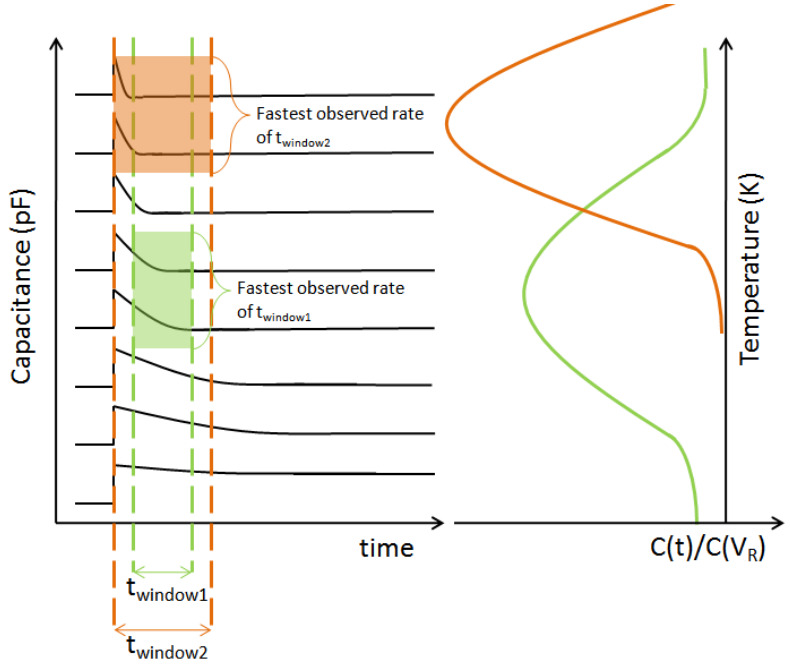

Figure 26: Illustration of multiple DLTS spectra, where the peak energies are shifted in intensity and versus temperature by changing the size of the time window over which the capacitance transient, $C(t)$ is observed.

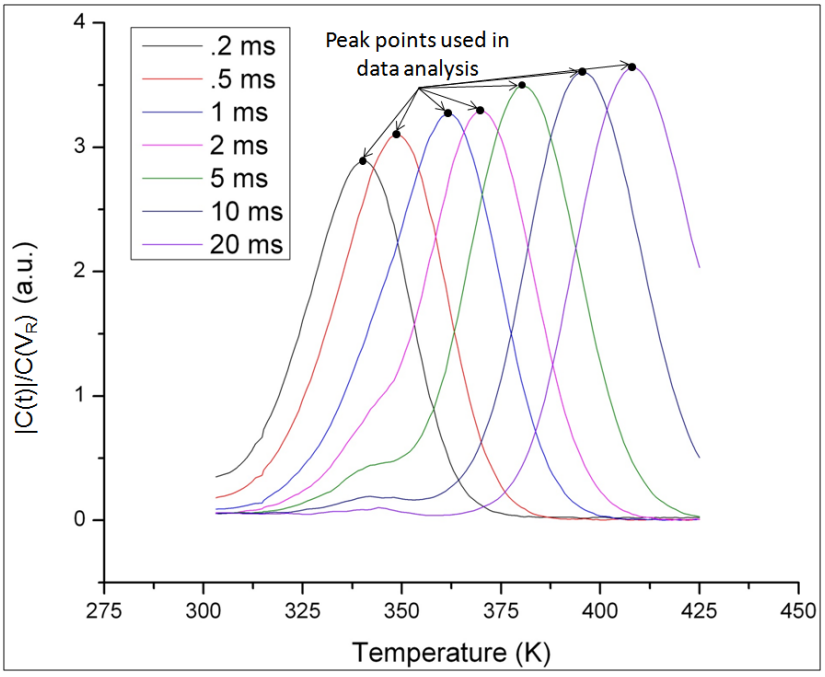

Figure 27: DLTS spectra of a GaAs diode taken with multiple varying rate windows with V_R=-3.0 V and V_P=+2.5 V. The peak points of the normalized capacitance transient, $C(t)/C(V_R)$ and their corresponding temperature values are used in the data treatment following to extract trap capture cross section, σ_n and apparent activation energy, E_a.

To examine this data and extract the last two trap parameters of capture cross section, σ_n, and activation energy, E_a, detailed balance gives the thermal emission coefficient from a deep level as below[80],

$$e_n = \left(\sigma_n < v_n > \frac{N_c}{g_n}\right) \exp\left(\frac{-\Delta E}{kT}\right) \qquad \textbf{Equation 29}$$

where σ_n is the majority-carrier capture cross section, $< v_n > = \sqrt{3kT/m_c}$ is the mean thermal velocity of minority carriers, $N_c = 2\left(2\pi m_{de} kT/h^2\right)^{3/2}$ is the effective density of states in the minority-carrier band, g_n is the degeneracy of the trap level, ΔE is the energy separation between trap level and the majority carrier band, T is the temperature, and k is Boltzmann's constant. In this case ΔE is taken as the apparent thermal activation energy of the trap, E_a.

The exponential relation between e_n and $1/T$ can be exploited if several spectra of C(t) are taken versus temperature with different transient windows. The peaks in these spectra as pictured in Figure 27 and related to Equation 29 above may be used in an Arrhenius plot to extract trap activation energy and capture cross-section. The log-linear plot follows as $\ln\left(T^2/e(n)\right) vs. 1000/T$ where $\ln\left(T^2/e(n)\right) = -\ln\left(e(n)/T^2\right)$ produces a positive slope, T^2 represents the temperature dependence of the mean thermal velocity ($T^{1/2}$) and the density of states ($T^{3/2}$) combined, and $e(n)$ represents the thermal emission coefficient at different peak points with integer index n=1,2,3,(…); the

unknowns in Equation 29 taken to be σ_n and ΔE. Relating the thermal emission coefficient to the Arrhenius plot, a general form of Equation 29 can be written as follows,

$$\frac{T^2}{e(n)} = \beta \exp\left(\alpha * \frac{1000}{T}\right) \quad \textbf{Equation 30}$$

where β is related to known parameters $< v_n > {}^{N_c}/_{g_n}$ and the yet-unknown apparent capture cross section, σ_n, and α is related to the known parameter of ${}^{1}/_{k}$ and the unknown apparent activation energy, E_a. Note, E_a is equivalent to $E_a' + \Delta E_\sigma$ where E_a' is the energy needed to get to the CB and ΔE_σ is the energy barrier of the apparent capture cross section, σ_n which is equivalent to $\sigma_{n0}\exp(-\Delta E_\sigma / kT)$. Thus capture cross-section has temperature dependence itself. In this study, ΔE_σ is assumed negligible.

A linear fit to the Arrhenius plot yields $y = ax + b$ where a is the slope and b is the intercept of the fit line. These can be related to the thermal emission equation as follows,

$$\ln\left(\frac{T^2}{e(n)}\right) = a\left(\frac{10^3}{T}\right) + b \quad \textbf{Equation 31}$$

where β and α can thus be described in terms of the line fit parameters as,

$$\beta = \exp\left(intercept, b\right) \quad \textbf{Equation 32}$$

$$\alpha = (slope, a) * 1000 \quad \textbf{Equation 33}$$

The fit slope and intercept values finally yield the capture cross and activation energy as below,

$$Capture\ Cross\ Section\ (cm^2), \sigma_n = 1/(5.917x10^{21} * \beta) \quad \textbf{Equation 34}$$

$Activation\ Energy\ (eV), E_a = (8.62x10^{-5}) * \alpha$ **Equation 35**

where the numerical values represent the aforementioned constants contained in β and α. In the software used for evaluation, the value $(m_{de}^3/m_C)^{1/2}$ (contained in the density of states term, $Nc = (2.511 \times 10^{19}\ cm^{-3})\ (T / 300\ K)\ m_{de}^{3/2}$ and the thermal velocity term, $< v_n > = \sqrt{3kT/m_c}$) is simplified by assuming the effective mass value for Silicon for both the density of states effective mass in the conduction band, m_{de} and the carrier effective mass, m_C. This value is treated as a constant applicable to all materials and both bands, the supposition being that the measurement error exceeds the accuracy gained by using a more exact calculation. Thus all three apparent deep level parameters of trap concentration, N_t, capture cross section, σ_n, and activation energy, E_a are derived.

Although DLTS can also be used to measure minority carrier traps, the experimental techniques used in this study only examine majority carrier traps. Hence the detailed theoretical treatment of minority carrier trap parameters related to capacitance transients will be omitted. In general, the theory becomes slightly more complicated due to the difficulties associated with completely filling the traps. Using a constant forward bias as opposed to V_R, holes are injected into the n-type side and can become trapped by deep levels. The theoretical analysis follows the dual of the majority carrier emission analysis above (now eliminating those parameters in Equation 17 that are negligible in the hole emission process), but the hole traps will only saturate if hole capture dominates both electron capture and hole emission, *i.e.* $c_p p >> e_p + c_n n$, which may be difficult to achieve in the n-type material.

3.3 Experimental

3.3.1 Sample Review

As put forth in the introduction section 1.4, the samples used for DLTS analysis comprise a set of two different stack structures (baseline and 1 layer QDs) and three different miscuts of the GaAs substrate (2*K*, 6*K*, and 6*N*), for a total of six samples. Sumitomo Electric provided the 2” diameter, approximately 350 μm thick, n^+-type (Si doped) GaAs substrates used in this research. Each sample was halved, one half to be fabricated for DLTS testing, the other reserved for optical probing. Schottky diode contacts were made with 500 nm thick gold circular pads on the halves for DLTS testing, designed to varying in diameter from 600 μm to 100 μm (with a tolerance of ~4 μm), and an image of a fabricated 600 μm diode is shown in Figure 28. Figure 28 below also shows one half-wafer which received the diode mask. Each section of the wafer has been categorized: near the flat (used as a reference for sample positioning during growth), middle, and away from the flat (bottom). The wafer may see *V-III* ratio variation across its surface during the growth process, thus the wafer sections were designated as in Figure 28. The diodes are distributed evenly across the wafer, and each diode was assigned a numerical designation for testing purposes.

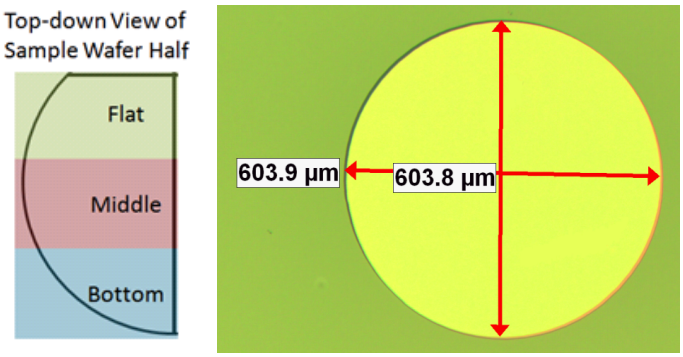

Figure 28: Left: Top-down view of the wafer half used in DLTS analysis, marked so as to designate different areas of the wafer. This is significant due to placement in the growth chamber, where the flat receives a different flow of *III-V* gas than the bottom. Right: microscopic image of a fabricated Schottky diode designed to be 600 µm.

The semiconductor stack used for each sample is pictured in Figure 7 for reference. This particular stack was chosen based on the limitations of the DLTS testing system used, where the capacitance meter can accurately read down to 10 pF and reaches its maximum at 1000 pF or 1 nF. Due to the capacitance limitation, the DLTS system can thus only probe down to a certain depth, based on the relation,

$$C = \frac{A * \epsilon_S}{W_D} \qquad \textbf{Equation 36}$$

where C is the capacitance, A is the area of the diode pad, and ϵ_S is the material dielectric constant (which is assumed to be 12.9 * 8.854x10^{-14} F/cm for GaAs[81]). From this the maximum probing depth of the system was found to be approximately 4000 nm for a 600 µm diameter diode and 1800 nm for a 400 µm diode, and hence the samples were designed so the semiconductor to be probed was safely within these depth limits. Lightly doped n-type GaAs was chosen as the material to be probed below and above the QD layer, and thus in the baseline samples, since the depletion width also follows the equation,

$$W_D = \sqrt{\frac{2\epsilon_s(\varphi_{bi}+|V_r|-\frac{kT}{q})}{qN_D}}$$ **Equation 37**

where ψ_{bi} is the built-in voltage (assumed to be between 0.9 V and 1.05 V for Au Schottky contacts on GaAs[81]), and N_D is the donor doping concentration. In order to reach the desired depth with a reasonable V_R the donor doping concentration was designed to be between 1x10^{16} cm^{-3} and 5x10^{16} cm^{-3}. The final doping of the n-type GaAs region above and below the QD layer (and in the top layer of the baseline samples) was approximately 4.5x10^{16} cm^{-3}, where the QD layer could be reached at reverse bias between 5 V and 6 V, corresponding to a depletion width (or probing depth into the semiconductor stack) of approximately 400 nm to 440 nm.

3.3.2 Current-Voltage Characterization

A material defect within a diode may be revealed by the current-voltage (*I*-*V*) characteristic by showing an ideality factor of $n \geq 2$ at low forward biases, where this ideality factor indicates increased recombination in the space charge region (SCR). Non-idealities in the material, such as defects (carrier-recombination centers that do not allow the carrier to be extracted as current), change the appearance of the current-voltage characteristic which, under non-ideal circumstances, follows the equation below[82],

$$I = I_0(e^{\frac{qV}{nkT}} - 1)$$ **Equation 38**

where *n* is the ideality factor. If *n*=1 the diode is ideal. In reverse bias the quality of a diode may be explored as well, where leakage current will increase incrementally as reverse bias increases. Every diode on the sample wafers was characterized using an

Agilent B1500 Semiconductor Parametric Analyzer to probe *I-V* in order to identify the non-ideal (n > 1.05) diodes. The n > 1.05 criteria for determining diode non-ideality was decided as 5% above the ideal case of n=1. All *I-V* curves were taken in the dark at room temperature. The diodes showing the strongest non-idealities were chosen as good candidates for deep level defects, as the higher ideality factor indicates non-radiative recombination in the SCR and thus a potential defect to be effectively probed by DLTS (being based on SCR modulation). Diodes showing ideal characteristics were tested as well to verify no DLTS signal could be observed.

The *I-V* information for the non-ideal diodes was plotted as the log of the absolute value of *I* versus *V* for determination of the Schottky barrier height and ideality factor in the forward bias region (shown in Figure 29), using the standard equation to fit a Schottky diode *I-V* curve as below[83],

$$I = AA^{*}T^{2}\exp(-\beta\varphi_{bn})\left[\exp\left(\frac{\beta V}{n}\right)-1\right] \qquad \textbf{Equation 39}$$

where A is the area of the diode pad, A^* is Richardson's constant (assumed to be 8.4 A/cm^{2}K^2 for GaAs[84]), β is the inverse thermal voltage or q/kT, ψ_{bn} is the Schottky barrier height, V is the applied forward bias, and n is the ideality factor.

The total amount of diodes showing non-ideal *I-V* characteristics (*i.e.* n > 1.05 and tagged as non-ideal) were summed in the different regions of each wafer, and divided by the total amount of diodes in that region to arrive at a percentage of diodes with non-ideal characteristics and to observe how this non-ideal distribution changed across samples and across the wafer itself. The results of this analysis are tabulated below,

where the miscut is noted in the sample title as well as its designation as a baseline sample (labeled base) or a 1 layer QD sample (labeled 1x).

Table 4: The percentage of non-ideal diodes found in *I-V* characterization categorized by location on the sample.

Sample	Position on the Wafer	% Non-ideal Diodes found
2Kbase	flat middle bottom	17% 22% 17%
6Kbase	flat middle bottom	17% 0% 0%
6Nbase	flat middle bottom	56% 56% 21%
2K 1x	flat middle bottom	0% 0% 17%
6K 1x	flat middle bottom	8% 17% 11%
6N 1x	flat middle bottom	28% 17% 17%

It can be noted from this analysis that the 2*K* and 6*K* samples have less percentage of non-ideal diodes than the 6*N* samples. Also, the non-ideal diode distribution in the 6*N* samples is fairly uniform across the wafer, whereas in the 2*K* and 6*K* one-layer (1x) QD samples, the defect distribution is heavier away from the flat (at the bottom). Also the addition of quantum dots seems to actually improve material quality in the 6*N* samples, where the 6*N* 1x sample has less non-ideal diodes on a percentage basis than the baseline sample. The prevalence of diodes with $n \geq 1.05$ may

not indicate a defect, however, and could be processing related. Further analysis with DLTS will help better determine the defective characteristics of these samples.

In the 2*K* and 6*K* baseline samples, no ideality factors greater than n=1.17 were found. For the 2*K* and 6*K* 1x, one diode on each wafer was identified away from the flat (near the bottom) with $n \geq 2$. The *I-V* data and fits for each of the 4 diodes identified as having the highest ideality factor for the 2*K* and 6*K* samples are pictured in Figure 29.

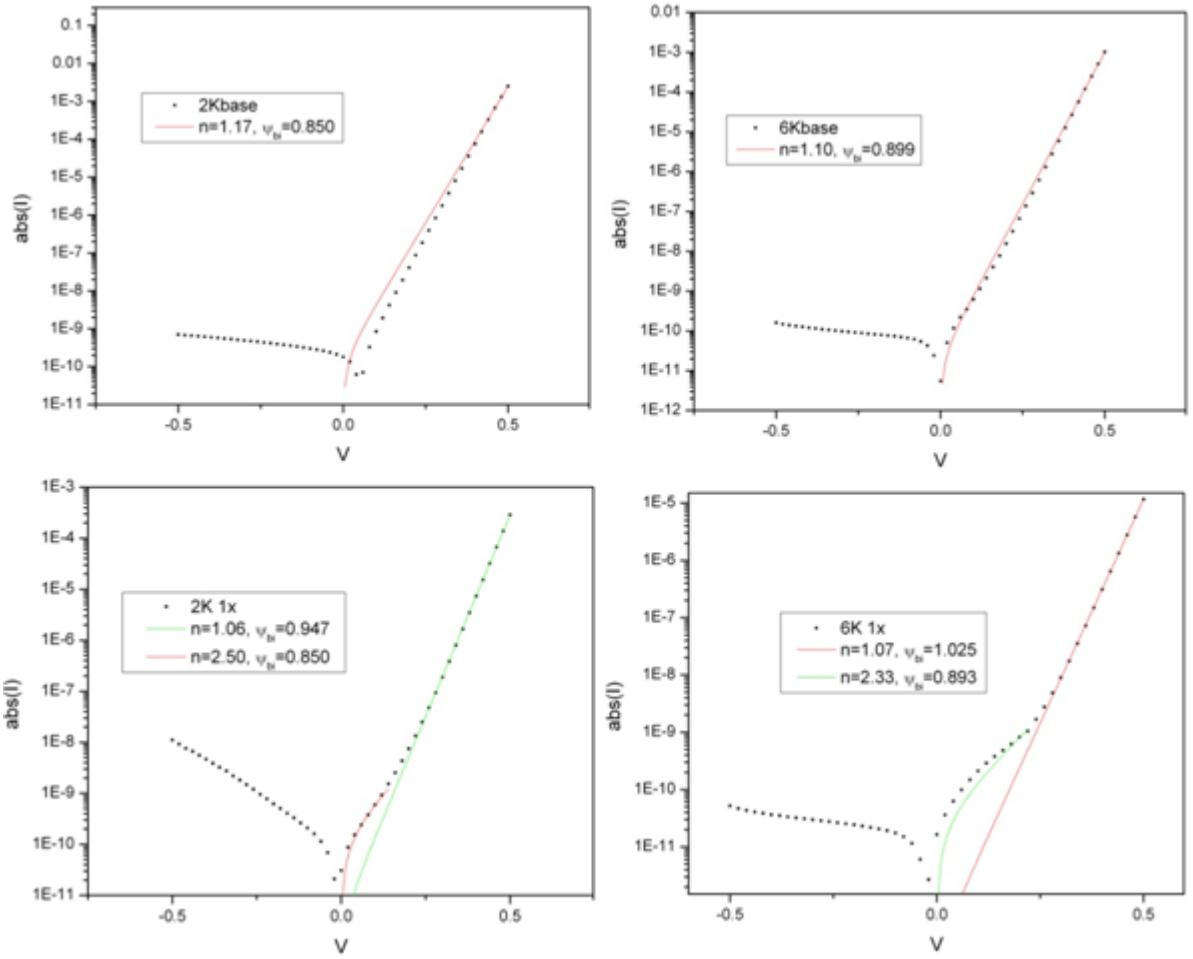

Figure 29: *I-V* analysis for the 2*K* and 6*K* baseline and 1x samples. The calculated ideality factors and built-in potential associated with each fit are displayed on the graph.

Note that for the 1x diode curves, the *I-V* characteristic recovers to an ideality factor of n=1 at higher forward bias as diffusion begins to dominate recombination in the SCR, *i.e.*, state filling occurs in the SCR due to increased carrier injection. Also, the leakage current in reverse bias shows a deviation from the ideal Schottky diode, as leakage current increases steadily with higher V_R.

For the 6*N* baseline sample, the diodes having a high ideality factor (approaching n=2) were identified mainly in the middle of the wafer. However for the 6*N* 1x sample, no diode was identified with an ideality factor greater than n=1.13. The *I-V* plots and fitted values for the 6*N* samples with the highest ideality factors are pictured below.

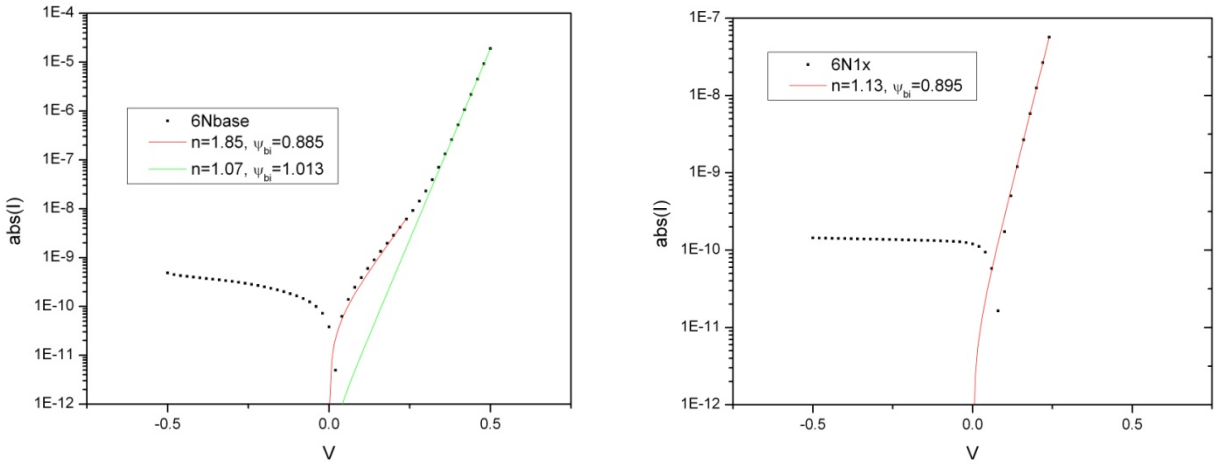

Figure 30: *I-V* characteristic for the 6*N* baseline and 1x samples.

Note that the leakage current for the 6*N* 1x diode is much steadier as V_R increases compared to both the 6*N* baseline sample and the 6*K* and 2*K* 1x samples. Also, the barrier heights measured tend to increase from the baseline samples to the one-layer QD samples, as tabulated below,

Table 5: Tabulated extracted values of Schottky barrier height, ψ_{bn} for all samples, taken from *I-V* analysis.

Degree Miscut	Baseline ψ_{bn}	QD ψ_{bn}	% Increase
2K	0.850	0.947	10%
6K	0.899	1.025	12%
6N	0.885	0.895	1%

The trend is slight, but is outside of the error (which is not more than 5% in all cases) of the fit from Equation 39 for the *2K* and *6K*. This indicates increased band bending as the conduction band increases in potential and may suggest shallower trap levels in the QD samples.

The results from *I-V* analysis show a greater concentration of diodes with non-ideal characteristics in the 6*N* baseline and QD samples, as seen in Table 4. Also it is noted that the concentration of defects in the 2*K* and 6*K* QD samples is weighted towards the bottom of the wafer, as opposed to a more even distribution in the 6*N* sample. From fits of the *I-V* curve using the Schottky diode current voltage relation, ideality factors for the diodes are obtained. The 2*K* and 6*K* baseline samples have diodes with ideality factor, $n \leq 1.17$ whereas the 6*N* baseline sample contained diodes with $n \leq 1.87$. Thus the 6*N* baseline sample diodes appear to be the most non-ideal overall. The opposite trend is observed in the QD samples, however, where the 2*K* and 6*K* QD samples have diodes with $n \geq 2$, and the 6*N* QD sample has diodes with $n \leq 1.13$. Hence simply taking the *I-V* data into account, the 6*N* substrate degrades the material grown above, and the QD layer actually improves material quality. Whereas in the 2*K* and 6*K* samples, the material grown on these substrates is initially relatively non-defective, but defects become more prominent once the QD layer is grown. Overall, the

K miscut samples may experience formation of incoherent QD islands or bunch due to higher step edges, as discussed previously.

The identified diodes were used in the DLTS analysis following for deep level identification (as a control, random ideal diodes were tested as well). It must be noted, however, that the diode coverage of the semiconductor surface was not complete. Only about 5% of the semiconductor surface has a diode pad, due to the metal pattern design. Thus although general conclusions based on Table 4 could be drawn concerning the overall semiconductor quality and the concentration of defects in a certain part of the wafer, due to the extent of surface it is very possible that a deep defects exists where no diode pad is found.

3.3.3 Capacitance-Voltage Characterization

Capacitance-voltage (*C*-*V*) analysis was also performed on diodes (ideal as well as those test candidates with non-idealities) where capacitance was monitored as a function of reverse voltage using the Agilent B1500 Semiconductor Parametric Analyzer. All *C*-*V* curves were taken in the dark at room temperature. This analysis allowed the extrapolation of sample doping, N_D, built-in voltage ψ_{bi}, and the verification of calculated depletion width values over reverse bias, V_R, verifying the probing depth. Using a plot of $1/C^2$ versus voltage, the doping can be extracted as,

$$N_D = \frac{2}{q\epsilon_s}\sqrt{-\frac{1}{d(1/C^2)/dV}} \qquad \textbf{Equation 40}$$

where the change in $1/C^2$ versus the change in voltage or $d(1/C^2)/dV$ can be found as the slope of a linear line, fitted to the $1/C^2$ plot. Also, ψ_{bi} can be determined from this linear fit, as the x-axis crossing (in the forward voltage region)[81].

Figure 31 is an example of the *C-V* data extracted, and also shows calculated depletion width values using Equation 36 for each data point taken. The extraction of W_D parameters allows the more accurate analysis of probing depth for DLTS investigation. The plots also compare diodes on the 2*K* and 6*K* 1x samples, showing data for good diodes (where n=1) and the bad or defective diodes selected for DLTS testing (where $n \geq 2$). These samples were chosen for this graphical comparison as the defective diodes found displayed the highest ideality factors of the sample set.

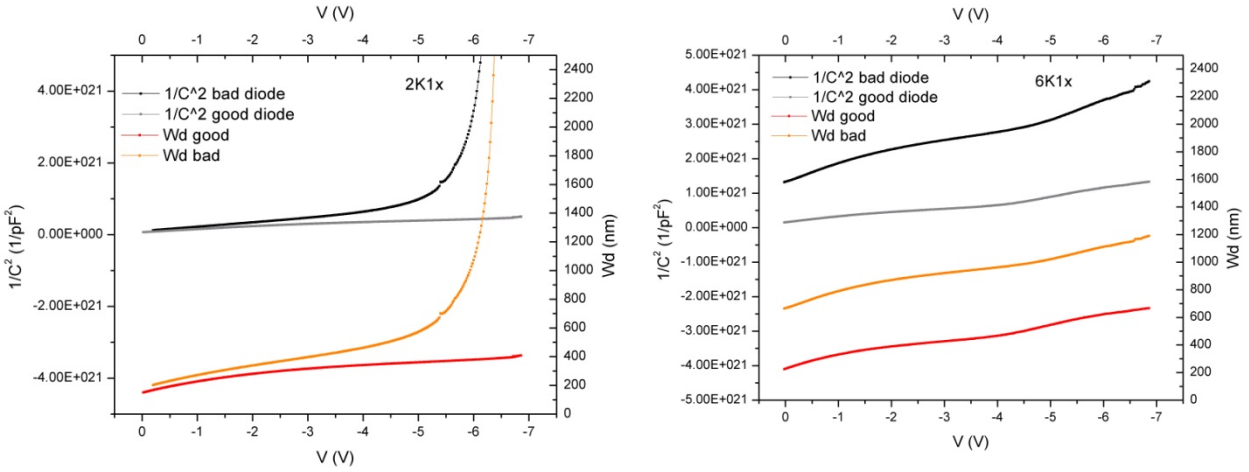

Figure 31: *C-V* characteristics of the 2*K* and 6*K* 1x samples, where 1/C2 and WD are plotted as a function of V_r. The graphs compare a non-ideal "bad" diode identified from *I-V* analysis with an ideal "good" diode of n=1.

Observe that for the defective diodes, the capacitance characteristic is lower in magnitude over reverse bias than the ideal case, corresponding to a greater depletion depth. In other words, the QD layer is reached faster with increasing magnitude of reverse bias than in the ideal diodes. Note that these plots are not linear with reverse bias, as would be contrary to expectations for uniform doping. This non-uniformity is attributed to the QD layer, which is reached approximately 400 nm to 440 nm below the semiconductor surface. Figure 32 illustrates the difference between the appearances of a uniform doping *C-V* characteristic as opposed to the QD sample characteristic. In the

2*K* samples compared below, it is observed that the QD layer is not reached in the range of reverse voltages shown for the QD sample.

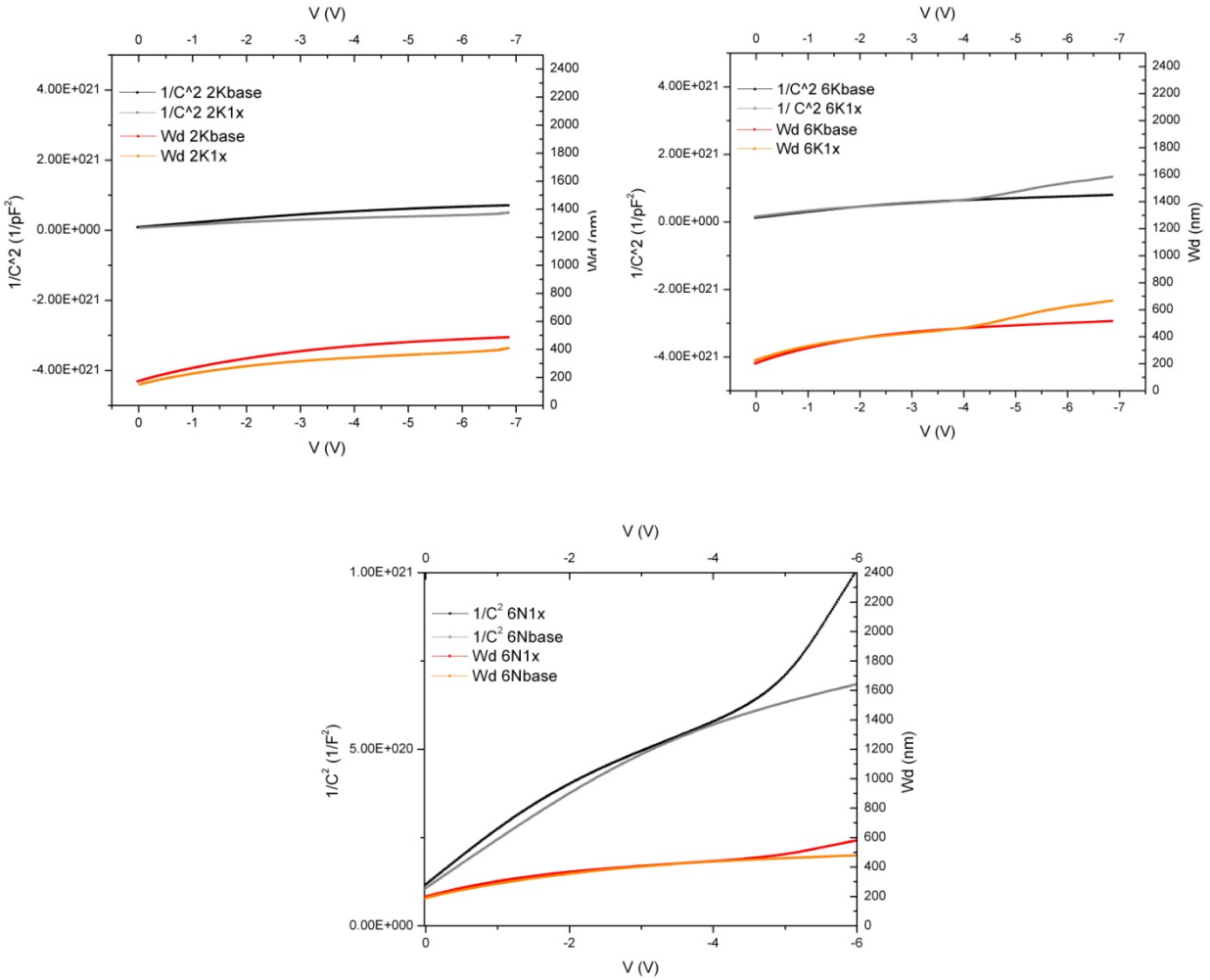

Figure 32: On the upper left, the 2*K* baseline sample and 2*K* QD sample are compared, where the linear $1/C^2$ trend indicates uniform doping. On the upper right and lower center graphs, this linear trend is also observed in the baseline samples; however, the kink in the QD samples at approximately -4.0 V reverse bias indicates the QD layer has been reached. This can be correlated to depletion depth, also plotted, where the QD layer is reached about 400 nm to 440 nm beneath the surface.

It is interesting to note that the 6 degree miscut samples deplete much faster with reverse bias than the 2 degree sample. This may be explained by the differences in n-type doping in the layer above the QDs.

To extract doping and built-in potential values, the most linear part of the curve was taken from the *C-V* plots for fitting, typically from 0 V to -1.0 V or -2.0 V, depending

on the linearity of the observed data. As the curve reaches greater reverse biases, some deviation from linearity can be seen, which could be attributed to the possible defect states, as well as an intersection with the QD area. In the 6*K* sample, the capacitance drops off much faster over increasing reverse bias than in the 2*K* sample, thus the depletion region reaches the QD layer faster with reverse bias and actually passes through that layer, as evidenced by the plotted depletion width values (the QDs are located ~440 nm from the semiconductor surface). This decay of capacitance in the 6*K* and 6*N* samples could be due to differences in leakage current, which appears to be higher in the 2*K* defective diode, as observed in *I*-*V* analysis in Figure 31. In general, the capacitance values are lower in the defective or bad diodes as compared to their ideal counterparts, thus the depletion region is extended more quickly with lower reverse bias. The results for doping values and built-in voltages are tabulated in Table 6; some of the samples selected for DLTS testing are highlighted as a comparison to the non-defective diodes (not highlighted). Standard error values were determined from the quality of the linear fit.

Several comparisons based on these extracted values can be made between samples and across the wafer of a single sample. First, the doping found in the 2*K* and 6*K* 1x defective diode samples is lower than the corresponding ideal diode that was measured on the same part of the wafer (see rows 2 & 3 and 7 & 8 in Table 6), which could be correlated to the lowering of effective doping due to a majority-carrier trapping. With a lower doping, one would suspect a lower built-in voltage. However, ψ_{bi} appears to increase from the ideal samples to the non-ideal.

Table 6: Tabulated *C-V* data, using a linear fit to extrapolate values.

Number	Sample	Position	Ψbi (V)	+/- (mV)	Doping (cm^{-3})	+/- (cm^{-3})
1	2K1x	flat	1.371	11	5E+16	4.65E+14
2	2K1x	bottom	0.820	1	4.1E+16	2.05E+14
3	2K1x	bottom	0.914	5	3.84E+16	1.14E+14
4	2Kbase	flat	0.783	0	4.46E+16	3.69E+13
5	2KBase	bottom	0.728	4	3.72E+16	8.80E+13
6	6K1x	flat	1.730	-9	8.88E+15	6.66E+13
7	6K1x	bottom	0.975	1	2.6E+16	1.87E+14
8	6K1x	bottom	1.116	-6	1.44E+16	1.26E+14
9	6Kbase	flat	0.727	1	2.35E+16	7.88E+13
10	6Kbase	bottom	0.674	1	2.24E+16	3.87E+13
11	6N1x	flat	0.761	0	1.91E+16	-3.98E+13
12	6N1x	bottom	0.745	0	2.70E+16	-4.71E+13
11	6Nbase	flat	0.757	0	2.87E+16	1.73E+13
12	6Nbase	bottom	0.753	0	2.67E+16	6.40E+12

Also, the 2*K* samples (both baseline and 1x) have almost twice the doping levels of either the 6*K* or 6*N*, which suggests differences in the Si_2H_6 incorporation due to local variation in *V-III* ratio following gas flow patterns in the growth reactor. Finally, across the individual wafers, an increase in doping from the bottom of the wafer to the flat is observed in general, excluding only the 6*K* and 6*N* QD samples. This is best illustrated in tabular form (see Table 7), where a percentage increase in doping from the bottom of the wafer to the flat is observed in all samples excluding the 6*K* 1x. The percent variation value shown in Table 7 is calculated as,

$$\%\,Variation = \frac{Doping\ flat - Doping\ bottom}{Doping\ flat} * 100 \qquad \textbf{Equation 41}$$

Table 7: Variation of doping across the sample wafers

Sample	Doping bottom	Doping flat	% Variation
2kbase	3.72E+16	4.46E+16	20%
6Kbase	2.24E+16	2.35E+16	5%
6Nbase	2.67E+16	2.87E+16	8%

Sample	Doping bottom	Doping flat	% Variation
2K1x	3.97E+16	5.00E+16	26%
6K1x	2.02E+16	8.88E+15	-56%
6N1x	2.70E+16	1.91E+16	-29%

Finally, an increase in ψ_{bi} from the bottom of the wafer to the flat follows the trend of increasing doping, corresponding to the changing Fermi level, E_{Fn} which is closer to the CB with higher doping and thus would pull the CB further down further.

3.3.4 C-V Summary

The observation that the doping values are greater near the flat of the wafer (see Figure 28 for wafer orientation), would correspond to enhanced Si-dopant incorporation towards the flat during growth. Also, the 6 degree samples reveal a doping of approximately half that of the 2 degree samples, which illustrates how Si-dopant incorporation is affected by miscut degree. Interestingly, the *C-V* profiles comparing non-ideal diodes on the 2*K* and 6*K* QD samples to ideal diodes measured on the same part of the wafer show a decrease in n-type doping, yet an increase in built-in voltage from the non-ideal to the ideal diodes. Finally, a point-by-point calculation of depletion width (inversely related to capacitance) is also plotted and it is revealed that the 6 degree samples deplete much faster with lowering reverse bias, thus the QD layer may be reached with less applied voltage, $|V_R|$. This corresponds to lower capacitance values (and thus doping) in the 6 degree samples.

3.3.5 DLTS Set Up

The experimental set-up described herein was assembled for the purposes of this study and is the only functioning DLTS system at Rochester Institute of Technology. For temperature-controlled experiments, the sample was placed in a Janis Cryogenic probe station cooled using liquid nitrogen (LN2), temperature controlled by a Lakeshore 331 TC, and brought to vacuum level (~1x10^{-6} mBar) by a Varian Turbo-V 81-AG pump. The sample was pulsed through the diode pad on top of the stack, or anode, and probed through the ground ohmic contact, or cathode. The Sula Technologies Basic DLTS Unit used includes: a pulse generator which produces a square-wave superimposed on a negative DC bias as well as the 1 MHz measurement signal used to determine sample capacitance (the pulsed bias voltage and the capacitance measurement signal are mixed before appearing at the pulse generator output); a capacitance meter consisting of a self-balancing bridge circuit which detects small, rapid changes in capacitance following a pulse and can also be used for static *C-V* measurements; and correlators which use a boxcar integration technique where the capacitance of the second correlator is subtracted from the first to yield the capacitance transient over the defined transient window, $t_2 - t_1$ (where $t_2 = 5.3*t_1$), and multiple rapid measurements are taken and then averaged. Finally, the signal is converted so as to be interpreted by the Sula DLTS Version X.8 computer software program as described in the theoretical development above, which produces a plot of the DLTS spectra, $\frac{|C(t)|}{C(V_R)}\ vs.\ T$. Figure 33 depicts the experimental set-up graphically. The Sula DLTS system is made up of several different components, as pictured in Figure 34.

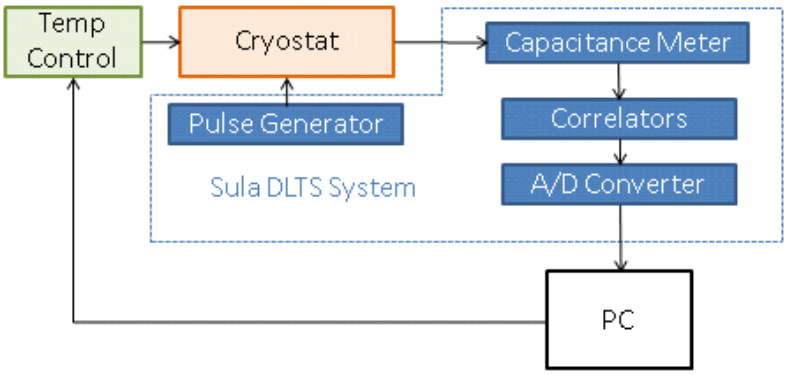

Figure 33: Block diagram of DLTS experimental setup.

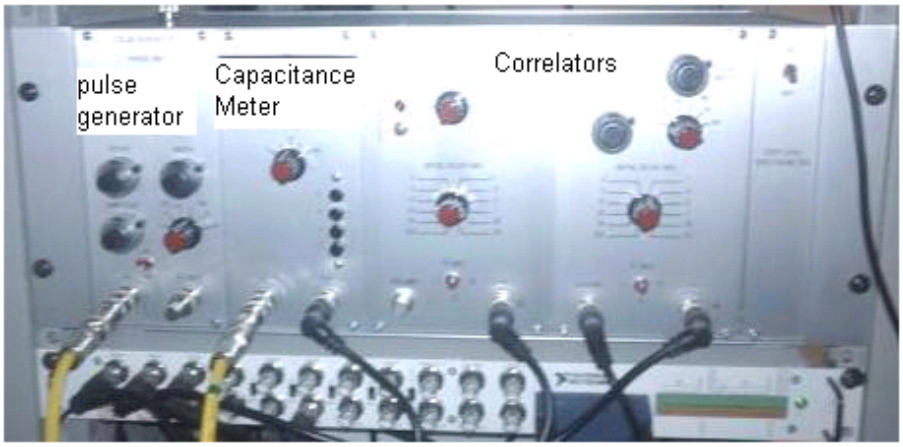

Figure 34: Full Sula DLTS system, including correlators, capacitance meter, and pulse generator.

The pulse generator and reverse bias settings are controlled by coarse adjust knobs, as seen in Figure 35. The period and width of the pulse generator can be set as well. In this study the pulse width was set at 1 ms to ensure complete filling of the traps states, with the period determined from the width of t_{window} in milliseconds as,

$$period = t_{window} * 10 + pulse\ width \qquad \textbf{Equation 42}$$

where the period is set within safe limits in order to obtain the capacitance transient within the designated rate window before the beginning of the subsequent pulse. On the

capacitance meter, as seen in Figure 35, a knob controls the range of capacitance displayed, where the capacitance measured follows,

$$Capacitance\ Measured\ (pF) = Range\ x\ Displayed\ Value \qquad \textbf{Equation 43}$$

The Sula manual generally recommends that the display reads between 0.1 and 1.0 for reliable measurements (insuring the meter does not overload or reach a value too low to measure). The push buttons, seen below the range knob on the capacitance meter in Figure 35, allow the user to view the reverse bias (marked as V), the leakage current (i), and the mixed output of the pulse generator (Π), *i.e.* the constant reverse bias overlaid with the filling pulse. The DLTS system can handle reverse leakage currents up to 150 μA.

Figure 35: Pulse generator module and capacitance meter for rate window control and transient measurement.

Finally, the output of the pulse generator module is fed to the anode of the sample being tested (or the Schottky contact diode pad on the surface of the sample), which is placed in the cryogenic station pictured in Figure 36 for probing. The cryogenic station contains four probe arms and two outputs to ground. The input of the capacitance meter leads from the cathode of the device (or the ground probe of the cryogenic station) and the output feeds the correlator module of the DLTS system, also pictured, which uses a boxcar integration technique to treat the signal and feeds the capacitance transient to the computer. The initial delay knob sets the width of t_{window} as discussed above, and the pre-amp gain knob picture in Figure 37 is not used in the DLTS set-up (it is used for a differential DLTS method, an option for the DLTS system). The DLTS software shows a real time display of the normalized capacitance transient, or $C(t)/C_{background}$ as the measurements are taken over a temperature range specified by the user.

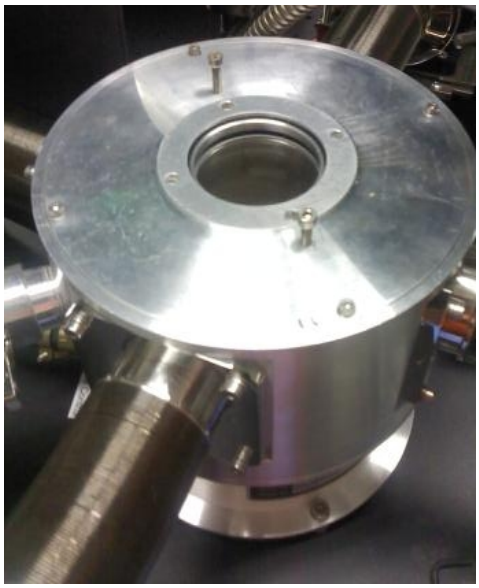

Figure 36: Cryogenic probe station. The sample is viewable through the window.

Figure 37: Correlator module on the DLTS system. The initial delay defines the size of t_{window} in milliseconds. The pre-amp gain knob is not relevant to the DLTS set-up here.

Once the samples are placed in the cryogenic chamber, a microscope is used to view the sample through the chamber window in order to contact the device. The output of the microscope is displayed on an LCD screen for accurate probing, as pictured below. Due to a drifting of the probe needle during testing resulting from temperature changes, the 100 μm devices were not tested in this study. In other studies, small diodes (less than 100 μm) are usually tested by wire bonding to the diode surface. However, this approach was not realized here.

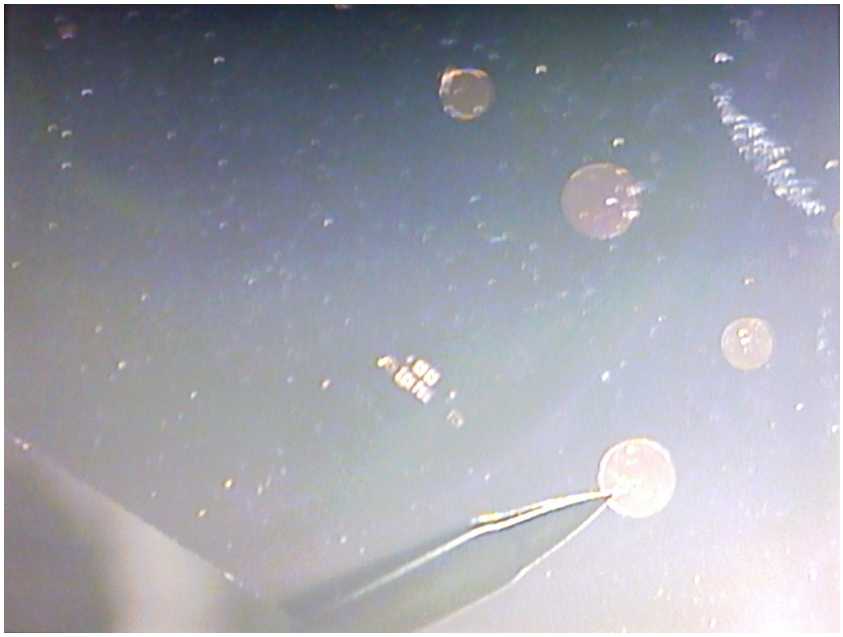

Figure 38: Output display of the microscope, looking down into the cryogenic chamber for diode probing.

3.3.6 DLTS Testing Results

Error for DLTS testing was characterized by observing the temperature hysteresis effects of the system, where the $\Delta C/C$ peak drifts slightly in subsequent measurements due to the lag between the thermocouple (placed very near the sample) temperature read-out and the actual sample temperature in the cryogenic chamber. This can be quantified by taking two temperature sweeps with the same rate window and biasing, noting the change in $\Delta C/C$ peak height and position with regards to temperature. For this analysis, it was found that the trap carrier concentration, N_t experienced an error of about 9%, as this value is based directly on the max capacitance peak height. The error values for capture cross section and activation energy were found to be about 4%.

As a preliminary test to verify the DLTS system operation, a lightly-doped n-type AlGaAs sample on the standard 2*K* GaAs substrate was tested, with the same fabrication methods applied as for the test sample set discussed previously in section 1.4. This sample was chosen as a well-known and prominent defect center is often found in AlGaAs. The DLTS spectra for multiple rate windows and the Arrhenius plot of the peak data are shown in Figure 39.

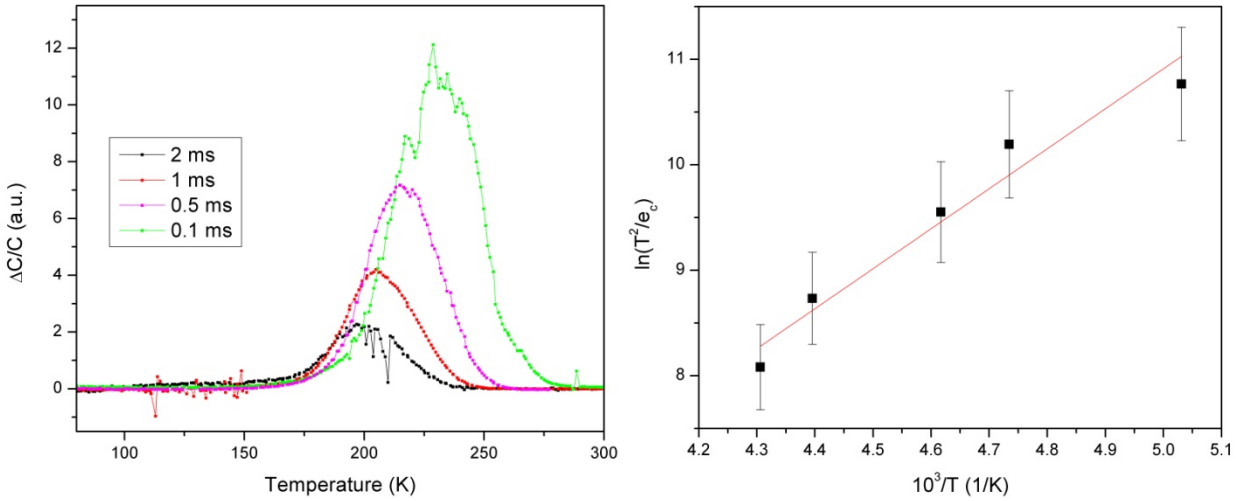

Figure 39: Left: Multiple DLTS spectra for the AlGaAs sample. Right: Arrhenius plot fit to the peak capacitance transient points.

The values extracted from the fit were capture cross section of ~5x10^{19} cm^{2}, a concentration of ~6x10^{15} cm^{-3}, and activation energy of 0.32 eV. This was identified as a *DX* center, so named due to an unknown “defect X” being coupled with an isolated donor in the semiconductor material, where the appearance of a deep state results from the band structure being modified by pressure or alloying, not necessarily the inhomogenity of the crystals[85]. This test successfully verified the operation of the Sula DLTS system.

3.3.7 DLTS Miscut Results

The 2*K* and 6*K* baseline samples did not reveal any deep level characteristics. Multiple diodes and areas of the wafer were tested, including those diodes that showed both ideal (n=1) *I-V* characteristics and those showing non-ideal ($n > 1.05$) characteristics, at different reverse biases and filling pulses, varying from -5.0 V to -0.2 V and +5.0 V to +0.2 V, respectively. Since no strong non-idealities were revealed for these samples in *I-V* characterization (*i.e.* $n \geq 2$) it is supposed that no prominent deep levels exist in the SCR which can be probed by the DLTS method.

The 6*N* baseline sample, however, did reveal non-idealities, with ideality factor approaching 2 (the maximum ideality factor found for this sample was n=1.87). The DLTS spectra for multiple rate windows taken by probing a defective diode for this sample are shown below. The reverse bias was held at -0.5 V, corresponding to a depletion region width of approximately 250 nm, and was pulsed with a filling voltage of +0.5 V. These values were chosen in order to stay within the limits of the DLTS system capacitance meter.

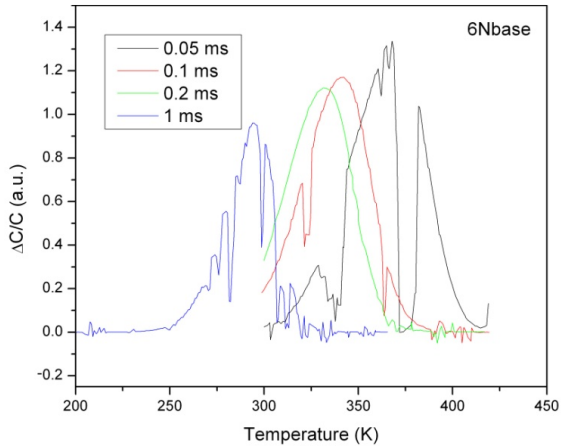

Figure 40: Multiple DLTS spectra taken at different rate windows for the 6*N* baseline samples.

Note that the peaks for the sample appear noisy. This can be correlated to the low capacitance values of the sample being probed, where gaps in the curvature indicate the capacitance transient was below the DLTS system's measurable value of 10 pF. The extracted peak points for this curve were used in a log-linear Arrhenius plot as described in the theoretical portion of this chapter, and were fit iteratively with a linear trend line, as shown below.

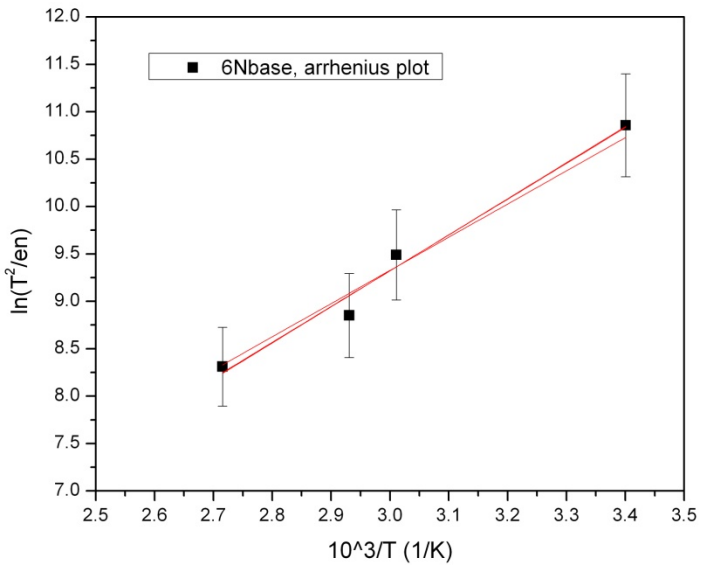

Figure 41: Arrhenius plots of the peak data extracted from DLTS probing of the 6*N* baseline sample.

The trap capture cross section and apparent activation energy were successfully determined from the intercept and slope of the fitted line, respectively. This data is shown in Table 8 below.

Table 8: Extracted capture cross section and activation energy observed above.

Sample	Capture Cross section	Plus/Minus	Activation Energy	Plus/Minus
	cm^2	cm^2	eV	meV
6N base	1.25E-21	5.00E-23	0.325	13

Note that the capture cross section for this deep level is small, correlating nicely to the ideality factor of n < 2 indicating a weaker defect, as well as the gaps seen in the spectra of Figure 40. This activation energy suggests a common GaAs deep level observed around 0.30 eV, named EL6 (see Appendix I)[66,86], and is similar to trap donor levels found in GaAs[87]. The trap concentration for this defect was determined from the maximum capacitance transient peak, obtained by probing the sample at lower reverse biases until the peak transient value did not change, indicating the trap was filled completely. The concentration for this trap was found to be 5.90×10^{15} cm^{-3} (+/- 5.31×10^{14} cm^{-3}) using Equation 28.

Other diodes probed on the 6*N* baseline sample showed even weaker characteristics of this defect (as indicated by the lower ideality factor, $n < 2$), where the gaps as seen in the curves of Figure 40 widened and the signal was unable to be resolved using different rate windows and reverse biases. An example of a noisy scan is shown below, where the small transients observed may indicate a peak (outlined in red), but do not conclusively indicate a strong deep level.

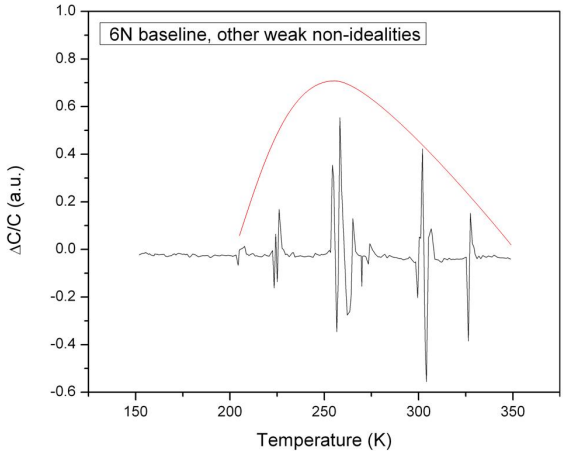

Figure 42: DLTS spectra characteristic of other non-ideal diodes probed on the 6*N* baseline samples. Although a noisy spectrum is observed, which may indicate a trap, the signal could not be resolved with the DLTS system.

Similarly, no strong defects were found in the 6*N* QD sample, which would be expected from the data presented in Table 4, as the 6*N* QD sample was in general less defective than the baseline sample.

The 2*K* and 6*K* one-layer QD samples, however, did show diodes with strong non-idealities in the SCR, with $n \geq 2$. These diodes were those away from the flat, near the bottom of the wafer where the greatest concentration of non-ideal diodes exists in both samples, as evidence by Table 4. For the 2*K* QD sample a -0.2 V reverse bias was used to probe the level with a +0.2 V filling pulse. This level was chosen to insure the capacitance transient for the deep trap did not saturate the DLTS capacitance meter, and also to insure the diode did not break down. This corresponded to a depletion width (calculated using Equation 36) of about 180 nm, thus scanning the semiconductor from the surface to about half-way down to the QD layer. The DLTS results for multiple rate windows are shown in Figure 43.

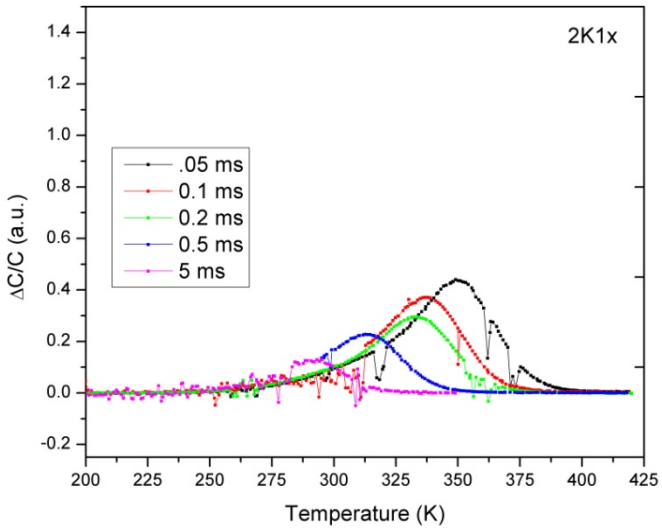

Figure 43: Capacitance transient characteristic for varying rate windows, t_{window} for the 2*K* QD sample using a -0.2 V reverse bias and a +0.2V filling pulse modulation.

For the 6*K* QD sample a -0.5 V reverse bias was used to probe the level with a +0.5 V filling pulse. This reverse bias is slightly higher in this sample to observe stronger defect characteristics. This corresponded to a depletion width (calculated using Equation 36) of about 400 nm, thus scanning the area just above the QD layer to the surface of the sample. The DLTS results for multiple rate windows are shown in Figure 44.

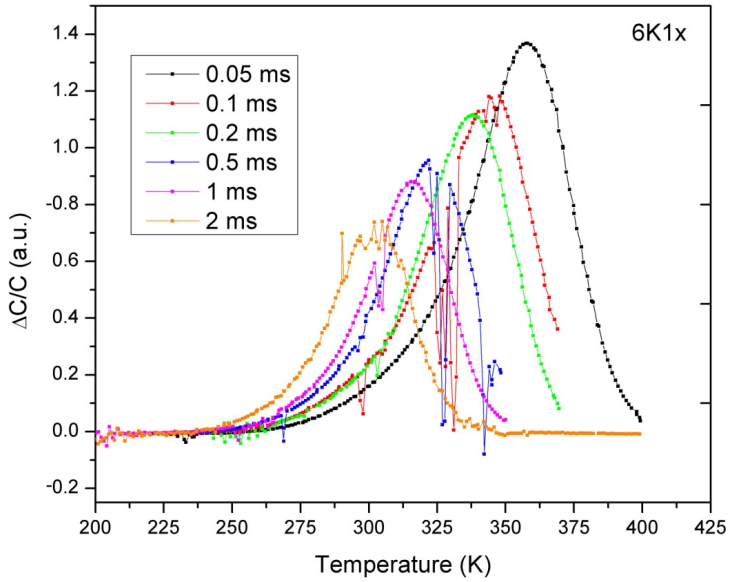

Figure 44: Capacitance transient characteristic for varying rate windows, t_{window} for the 6*K* QD sample using a -0.5 V reverse bias and a +0.5V filling pulse modulation.

The change in peak transient intensity from the 2*K* QD sample to the 6*K* QD sample is most likely a function of the differences in probing depth, as the 6*K* sample depletes more quickly with reverse bias. The peak data values for each transient window seen in Figure 43 and Figure 44 were used in the log-linear Arrhenius plots to extract capture cross section and trap activation energy as seen below. The plots were fit with a linear trend line iteratively to minimize fit error. The deep level activation

energies and cross sectional area are tabulated below, extracted from the best linear fit of the above plots.

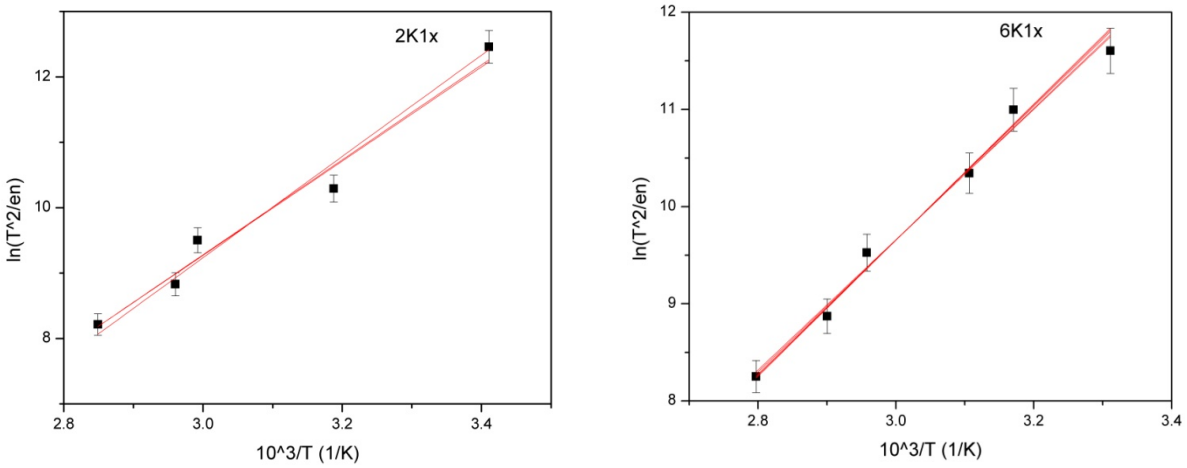

Figure 45: Arrhenius plots of the peak data extracted from DLTS probing of the 2*K* and 6*K* QD samples.

Table 9: Extracted trap parameters for the deep levels found in the 2*K* and 6*K* QD samples.

Sample	Capture Cross section	Plus/Minus	Activation Energy	Plus/Minus
	cm^2	cm^2	eV	meV
2K 1x	4.54E-17	1.81E-18	0.626	25
6K 1x	1.03E-17	4.11E-19	0.602	24

The concentration profile for these traps was extracted by probing the sample at lower reverse biases until the transient reached a maximum peak, indicating the trap was completely filled. The concentration data for these deep levels is tabulated below.

Table 10: Trap concentration extracted for the deep levels found in the 2*K* and 6*K* one-layer (1x) QD samples.

Sample	Trap Concentration	Plus/Minus
	cm^{-3}	cm^{-3}
2K 1x	2.35E+15	2.12E+14
6K 1x	1.17E+16	1.05E+15

The traps display very similar characteristics, with apparent activation energies between 0.60 eV, and much greater capture cross sections than those observed in the 6*N* baseline sample (about four orders of magnitude larger), suggesting an extended dislocation. The size and concentration of these traps could account for the changes in doping and built-in voltage revealed for the defective diodes in *C-V* analysis (see Table 6). Also, this activation energy does not correlate well to any common levels seen in GaAs (see Appendix I), especially the dominant EL2 level around 0.80 eV. To determine the origin of this deep level, whether originating from the QD layer or below the QD layer, spatial profiling of the sample was performed. Such a profiling can be realized by using different reverse biases to probe the sample down to a known depth, and choosing a filling pulse so as to only observe those defects residing in a certain region of the semiconductor stack, *i.e.* above the QD layer, around the QD layer, or below the QD layer. The *C-V* data for both the 2*K* and the 6*K* sample was examined in order to selectively control the probed region for each sample, as shown in Figure 46. The region below the QDs corresponds to a probing region depth of approximately 500 nm to 600 nm. To probe through the QD layer, a reverse bias and filling pulse was chosen for each sample so as to probe between 400 nm and 460 nm below the semiconductor surface. Finally the region above the QDs was probed, corresponding to a depletion depth of about 400 nm.

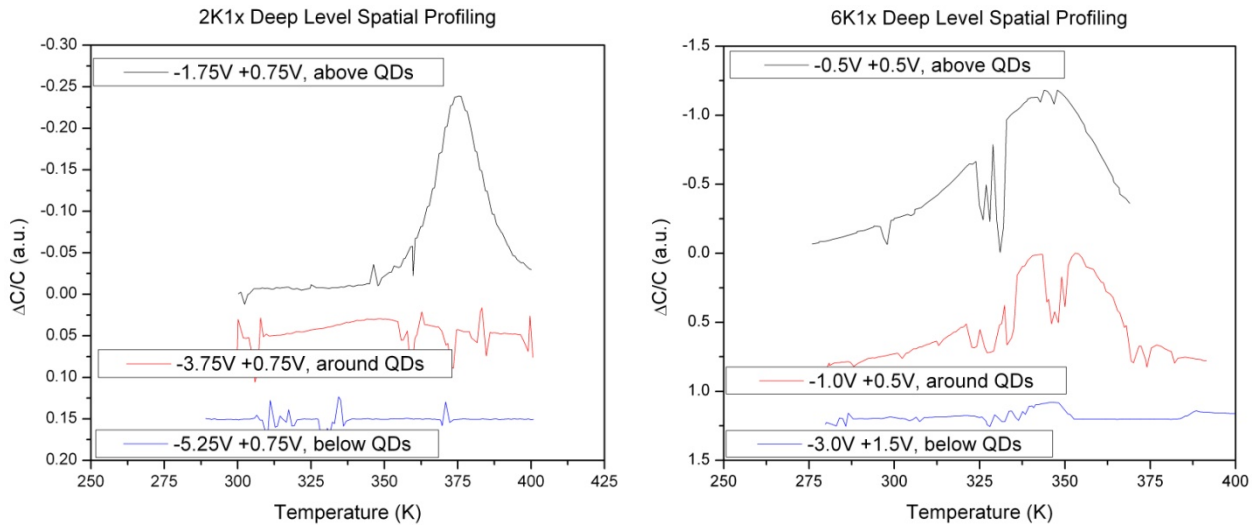

Figure 46: Depth profiling of the deep level defect observed in both the 2*K* and 6*K* QD samples. Reverse biases and filling pulse magnitudes were chosen based on the probing depth desired to be achieved.

Note that the reverse bias required to reach the QD layer (pictured in Figure 46 is lower for the 2*K* QD sample, which corresponds to the differences in doping seen in the *C-V* profiling. Also, the 6*K* sample DLTS signal is much more prominent, corresponding to the order of magnitude higher concentration shown in Table 10. Most notably, the transient disappears below the QD layer, and appears in scans around the QD layer, suggesting that this deep level originates from the QDs. In the 2*K* QD sample, the peak of the transient in the QD layer is not aligned with the peak above the QD layer, which could indicate the defect peak signal above the QD layer is a combination of two thermally active defects, or that the QD layer seeded one type of defect that acted a catalyst for the formation of the second extended defect through the top layer.

3.3.8 DLTS Miscut Results Discussion

In DLTS analysis, no deep level transient is resolved for diodes with an ideality factor, $n \leq 1.87$. Thus the 2*K* baseline, 6*K* baseline, and 6*N* QD samples have no corresponding deep level data to be discussed. The 6*N* baseline sample, however, reveals a trap level that is small, with a capture cross section of about 1.2×10^{-21} cm^2.

The sample was probed approximately 250 nm below the surface and an Arrhenius plot of the peak points observed over multiple transient windows allowed the extraction of the capture cross section and the activation energy, which was revealed to be about 0.33 eV. This energy level corresponds to a common GaAs deep level defect termed EL6[66]. This is one of the three most common deep levels found in GaAs and is categorized as a medium deep donor level that displays *DX* characteristics[86]. *DX* centers are so named due to an unknown "defect X" being coupled with an isolated donor in the semiconductor material, where the appearance of a deep state results from the band structure being modified by pressure or alloying, not necessarily the inhomogenity of the crystals[88]. Since this defect was only found in the 6*N* baseline material, it may be concluded that the miscut off the (100) surface toward the [111] direction (of the Ga terminated face) is generally less favorable and more prone to the development of such *DX* centers. As mentioned above, the 6*N* QD sample not only had more ideal diodes as seen in *I-V* analysis, but correspondingly revealed no prominent deep levels, thus the material quality is actually improved by the introduction of QDs. Thus it may be said that the QD layer suppresses the propagation of this defect through the semiconductor grown above.

Further DLTS analysis shows strong deep levels in the 2*K* and 6*K* QD samples near the bottom of the wafer (away from the flat), with activation energy around 0.62 eV to 0.60 eV, respectively. This level does not correlate well to any trap levels commonly found in GaAs, notably EL2 at ~0.80 eV, EL3 at ~0.55 eV and EL6 at ~0.30 eV[66,86]. The capture cross section of this trap was many magnitudes greater than the level revealed in the 6*N* baseline sample and the capacitance transient response for this deep level

was thus much stronger. The concentration of this defect in the 6*K* QD sample was higher by an order of magnitude (~1x10^{16} cm^{-3}) as compared to the 2*K* sample (~1x10^{15} cm^{-3}). A depth profiling of both samples revealed that the defect was visible in spectra in the layer above the QD layer and through the QD layer, but not below. This indicates the defect originates from the QD layer and is a result of QD growth. In a similar study, Asano *et al.* (2010) [71] probed QD InAs/GaAs QDs of similar structure to find levels associated with the semiconductor above and through the QD layer around 0.71 eV and 0.44 eV activation energies. Also, Lin *et al.* (2005)[89] found a deep level at ~0.50 eV in a similar QD system and Kim *et al.* (2009)[90] found a 0.60 eV level they termed a "native defect". The farthest any researcher has gone to explain the actual origin of these defects was Kaniewska *et al.* (2005)[92]. They found a level at 0.57 eV termed an "intrinsic point defect-oxygen complex", and went further to say deep levels around the QD layer formed during a growth interrupt between GaAs buffer layer growth and the InAs QD layer growth, enhancing incorporation of excess As and background impurities. Note that this defect is not found in the 6*N* QD sample, where the *N* miscut may suppress formation of this specific deep level.

Chapter 4

Conclusions, Summary and Future Work

4.1 Defect Mechanisms and Changes in Optical Material Characteristics

Optical probing, serving as a complement to defect identification where the actual energy transitions within the material are observed, reveals that the 2 degree sample forms QDs with significantly higher radiative recombination, correlating to higher photovoltaic conversion efficiency, where the inverse of a radiative process is the absorption of photonic energy. With low PL signals, the 6 degree samples show less radiative recombination, indicating more non-radiative recombination as would be observed in the SCR of the material.

From *I-V* and DLTS analysis of the sample set, the 2 degree and 6 degree sample with a miscut off the (100) lattice toward the [110] plane display similar characteristics in defect concentration across the wafer and deep levels detected. The 6 degree baseline and QD samples miscut off the (100) toward [111] plane show uniform defect distribution across the wafer and with a higher ratio to semiconductor material (see Table 4). This would suggest different mechanisms govern the defect behavior of the *N* and *K* miscuts, regardless of degree.

From *C-V* analysis, a correspondence between both 6*K* and 6*N* miscuts does exist, where doping is half of that seen in the 2 degree sample, indicating less Si inclusion. Also an opposite trend than that seen in the baseline 6 degree samples (doping increasing from the bottom of the wafer to the flat) is observed across the 6 degree one-layer QD samples, as seen in Table 7. This suggests that from the 6 degree baseline to the 6 degree QD samples, Si incorporation characteristics have changed.

Thus the decline in radiative recombination in the 6 degree samples as a result of Si incorporation issues is highly probable, as opposed to an increase in material defects in the 6 degree material. Thus, the decline in the 6 degree samples' PL signals may not be due to an increase in extended defects above the QD layer (recall Lobo *et al.* observed strong radiative emission from QDs, even after formation of a dislocation array[51]). Other studies suggest that a sharp drop in luminescence intensity from InAs/GaAs QDs is associated with increasing density of incoherent InAs islands, citing these incoherencies as being optically inactive[91]. Thus the 6 degree miscut samples may be prone to this type of incoherent QD formation.

4.2 Summary

The application of advanced *III-V* nanostructures is discussed with regards to optoelectronic device operation, and specifically the QD structure is examined in detail. The ability of this material to realize the intermediate band solar cell (IBSC) concept as proposed by Marti and Luque is also explored. The dependence of QD formation on lattice nucleation sites generated by the underlying substrate, limitations of QD formation and possible associated defects are also presented. The specific effects of substrate miscut on QD traits is thus proposed, and previous PL data from Hubbard *et al.*[38] establishes the precedent of a 2 degree miscut performing much better with regards to radiative processes than 6 degree material.

A sample set with varying miscuts of 2 and 6 degrees off the (100) lattice toward the [110] plane and 6 degrees off the (100) toward [111] plane is developed with an n-type GaAs baseline and a one-layer InAs/GaAs QD system capped with 400 nm of n-type GaAs. This sample set is examined with PL and displays the same characteristic

behavior discussed above. A PR signal is obtained for the 2 degree miscut sample which reveals lower-order, higher energy QD transitions than the ground state at 1.16 eV.

Schottky diodes are formed on the samples to electrically probe the material for deep defects using a DLTS system. The diodes are characterized by *I-V* and *C-V*, revealing non-idealities and doping characteristics. The 2*K* and 6*K* samples show very similar defect ratios across the semiconductor surface, as well as deep level characteristics with the one-layer QD samples showing a defect with activation energy ~0.60 eV which originates at the QD layer and propagates through the layer above. The 6*N* sample in general appears the most defective, and the baseline sample shows a weaker defect with activation energy of 0.33 eV, identified as the common GaAs defect EL6. The 6*N* QD sample is less defective than the corresponding baseline, and no deep level defects are found, suggesting that the QD layer improves the semiconductor material quality above the QD. Differences in the defect properties of the *K* and *N* miscut samples, regardless of miscut degree, implies that the defect-formation mechanisms present in these samples differs and is dependent on the crystallographic direction of the cut.

As no common defect mechanism between the 6*K* and 6*N* samples is established, it is supposed that the reduced PL signal (and thus radiative recombination) in the 6 degree samples is governed by Si incorporation compared to the 2 degree samples. This is assumed by the observation of the marked disparity in doping concentrations across the wafers of the 6 degree QD material as opposed to the baseline samples and the 2 degree QD sample. The differences in dopant incorporation

could imply a changing atomic step surface, or may increase formation of incoherent QD islands.

4.3 Future Work

Although extremely versatile, the DLTS method only reveals trap parameters as opposed to their cause or origin, thus further work should be done to resolve the defects further. DLTS probing of the layer around the QD region may reveal seeding traps with activation energies different than those found in the extended defects above the QD layer (as may be indicated in the 2*K* QD depth profiling), and thus give clues as to the formation of these deep levels. DLTS tests examining a more varied set of miscut samples may help uncover the origin of the deep level seen in the *K* miscut samples, paired with other evaluation methods, such as secondary ion mass spectroscopy (SIMS) to determine molecular composition of the semiconductor surface. Using DLTS to examine changing growth interrupt times and temperature could resolve the deep level evolution of these defects as well and help optimize the growth process. Atomic force microscopy (AFM) studies of the surface of uncapped QD samples grown under the same conditions and miscuts could verify the suppostion of incoherent QD islanding in the 6 degree samples.

The PR system should be optimized further so as to detect changes in reflectance signals for the miscut samples and conclusively define the different QD energy states present. PR evaluation across the surface of the wafers, where multiple PR spectra are taken for different areas of the wafer creating an effective PR map, could also be paired with *I-V* and *C-V* analysis to determine the effects of Si

incorporation on QD size. PR could also be used to study the electric field changes, in the miscut samples (if any) and in QD samples with increasing number of layers.

Finally, in this study an *n-i-n* QD sample structure was developed to identify electron traps in the QD samples using DLTS. However as it pertains to many devices and especially solar cells, it would be very useful to test the majority and minority carrier traps in a *p-i-n* or *n-i-p* devices. As QDs are usually formed in the *i*-region of these junctions, the differing effects of a *p* or *n* base underlying layer on defect evolution in the *p* or *n* capping layer may deviate significantly from the results shown here.

The future of the PR and DLTS methods may be applied in a variety of ways, by observing changing optical and defect properties of QD material while varying number of QD layers, growth conditions, material factors, *etc.* This type of evaluation compared to the data already obtained may help develop a portfolio on optimized QDs.

Appendix I

Common GaAs Deep Levels, Literature Study

Source	Sample	Dopant	Donor Concentration cm^{-3}	Deep Level	Activation Energy eV	Ohmic Contact	Schottky Contact
2000 Kaniewska[92]	GaAs	Silicon	1.00E+16	EL10	0.17	AuGeNi	Au
2001 Kazukauskas[87]	GaAs		1.00E+14		0.22		
2001 Kazukauskas[87]	GaAs		1.00E+14		0.32		
2001 Kazukauskas[87]	GaAs		1.00E+14		0.37		
2002 Markov[93]	p-GaAS	Chromium	2.00E+16	EL2	0.43		Au
1974 Lang[77]	n-GaAs		5.00E+15		0.43		
2001 Kazukauskas[87]	GaAs		1.00E+14		0.47		
1990 Nishizawa[94]	p-GaAs	Zinc	2.90E+17	EL2	0.48		
2000 Kaniewska[92]	GaAs	Silicon	1.00E+16	EL4	0.52	AuGeNi	Au
2001 Kazukauskas[87]	GaAs		1.00E+14		0.54		
2002 Markov[93]	p-GaAS	Chromium	2.00E+16	EL2	0.65		Au
1990 Nishizawa[94]	p-GaAs	Zinc	2.90E+17		0.72		
1997 Halder[95]	n-GaAs	Silicon	1.52E+17	EL2	0.74		Au
2002 Markov[93]	p-GaAS	Chromium	2.00E+16	EL2	0.75		Au
1974 Lang[77]	n-GaAs		5.00E+15		0.76		
1991 Samara[96]	n-GaAs		1.00E+15	EL2	0.78	In	Au
1990 Nishizawa[94]	p-GaAs	Zinc	2.90E+17		0.90		
1990 Nishizawa[94]	p-GaAs	Zinc	2.90E+17		1.03		

Label (Fig. 1)	Reference and alternative labels	Activation energy E_{na}, eV	Emission section σ_{na}, cm^2	Observations	Possible comparisons
ET1	(14)	0·85	$6·5\times10^{-13}$	Bulk material	
ET2	(14)	0·3	$2·5\times10^{-15}$	Bulk material	
ES1	(13)	0·83	$1·0\times10^{-13}$	Bulk material	
EF1	(15)	0·72	$7·7\times10^{-15}$	Cr doped bulk mat.	
EI1	(20)	0·43	$7·3\times10^{-16}$	V.P.E. mat.	
EI2	(20)	0·19	$1·1\times10^{-14}$	V.P.E. mat.	
EI3	(20)	0·18	$2·2\times10^{-14}$	V.P.E. mat.	
EB1	(16)	0·86	$3·5\times10^{-14}$	Cr doped L.P.E. mat.	
EB2	(16)	0·83	$2·2\times10^{-13}$	As grown V.P.E. mat.	
EB3	(12) (E5)	0·90	$3·0\times10^{-11}$	Electron irradiated mat.	
EB4	(12) (E4)	0·71	$8·3\times10^{-13}$	Electron irradiated mat.	
EB5	(17) (M4)	0·48	$2·6\times10^{-13}$	As grown M.B.E. mat.	
EB6	(12) (E3)	0·41	$2·6\times10^{-13}$	Electron irradiated mat.	
EB7	(17) (M3)	0·30	$1·7\times10^{-14}$	As grown M.B.E. mat.	
EB8	(17) (M1)	0·19	$1·5\times10^{-14}$	As grown M.B.E. mat.	
FB9	(12) (E2)	0·18	Imprecise	Electron irradiated mat.	
EB10	(12) (E1)	0·12	Imprecise	Electron irradiated mat.	
EL1		0·78	$1·0\times10^{-14}$	Cr doped bulk mat.	
EL2	(10) (A)	0·825	$(0·8–1·7)\times10^{-13}$	V.P.E. material	EL2 = ET1 = ES1 = EB2
EL3	(10) (B)	0·575	$(0·8–1·7)\times10^{-13}$	V.P.E. material	
EL4		0·51	$1·0\times10^{-12}$	As grown M.B.E. mat.	EL4 = EB5
EL5	(10) (C)	0·42	$(0·5–2·0)\times10^{-13}$	V.P.E. mat.	EL5 = EB6(?)
EL6		0·35	$1·5\times10^{-13}$	Bulk material	EL6 = ET2
EL7		0·30	$7·2\times10^{-15}$	As grown M.B.E. mat.	EL7 = EB7; EL7 = EL6(?)
EL8	(18) (D)	0·275	$7·7\times10^{-15}$	V.P.E. mat.	
EL9	(18) (E)	0·225	$6·8\times10^{-15}$	V.P.E. mat.	
EL10		0·17	$1·8\times10^{-15}$	As grown M.B.E. mat.	EL10 = EB8
EL11	(18) (F)	0·17	$3·0\times10^{-16}$	V.P.E. mat.	EL11 = ET3 = EL10(?)
EL12	(18) (A')	0·78	$4·9\times10^{-12}$	V.P.E. mat.	EL12 = EB4(?)
EL14		0·215	$5·2\times10^{-16}$	Bulk material	
EL15		0·15	$5·7\times10^{-13}$	Electron irradiated mat.	EL15 = EB9
EL16		0·37	$4·0\times10^{-18}$	V.P.E. mat.	

Figure 47: Documented deep levels compiled from Lang and other sources[66]

References

[1] M. Henini, Handbook of Self Assembled Sc Nanostructures for Novel Devices in Photonics and Electronics, Netherlands: 208, pp. 1-50.
[2] G. W. Bryant,G. S. Solomon, Optics of Quantum Dots and Wires, USA:2005, pp. 1-31.
[3] J. Q. Liu, N. Kong, L. Li, F. Q. Liu, L. J. Wang, J. Y. Chen, and Z. G. Wang, Sc Science And Technology, vol. 25(7).
[4] Y.-J. Doh, J. A. van Dam, A. L. Roest, E. P. A. M. Bakkers, L. P. Kouwenhoven, and S. De Franceschi, Science, vol. 309(5732), pp. 272-275, 2005.
[5] X. Gao, Q. S. Kang, J. T. W. Yeow, and R. Barnett, Nanotechnology, vol. 21(28).
[6] K. L. Wang, D. H. Cha, J. L. Liu, and C. Chen, Proceedings Of The Ieee, vol. 95(9), pp. 1866-1883, 2007.
[7] G. W. Bryant,G. S. Solomon, Optics of Quantum Dots and Wires, USA:2005, pp. 315-343.
[8] M. Grundmann (Ed.), Nano-Optolectronics Concepts, Physics, and Devices, Germany: 2002, pp. 3-19.
[9] D. Bimberg, M. Grundmann, N.N. Ledentiv, Quantum Dot Heterostructures, England: 2001, pp. 277-300.
[10] M. Henini, Handbook of Self Assembled Sc Nanostructures for Novel Devices in Photonics and Electronics, Netherlands: 208, pp. 84-121.
[11] J. Zhang, Q. Li, X. W. Di, Z. L. Liu, and G. Xu, Nanotechnology, vol. 19(43), 2008.
[12] G. S. Solomon, J. A. Trezza, A. F. Marshall, and J. S. Harris, Physical Review Letters, vol. 76(6), pp. 952-955, 1996.
[13] G. W. Bryant,G. S. Solomon, Optics of Quantum Dots and Wires, USA:2005, pp. 435-478.
[14] M. Henini, Handbook of Self Assembled Sc Nanostructures for Novel Devices in Photonics and Electronics, Netherlands: 208, pp. 620-656.
[15] J. Phillips, Journal Of Applied Physics, vol. 91(7), pp. 4590-4594, 2002.
[16] M. Yamaguchi, *Scs*, vol. 33, no. 9, pp. 961-964, (1999).
[17] L. L. Kazmerski, *Journal of Electron Spectroscopy and Related Phenomena*, vol. 150, no. 2-3, p. 105, (2006).
[18] Christopher Bailey, Seth Hubbard, Stephen Polly, David Forbes, and Ryne P. Raffaelle, *Mater. Res. Soc. Symp. Proc*. 1121E, N10.2, (2008).
[19] Seth M. Hubbard, Christopher Bailey, Stephen Polly, Cory Cress, John Andersen, David Forbes, and Ryne Raffaelle, *J. Nanophotonics*, vol. 3, p. 3188 (2009).
[20] Nozik et al., *Physica E*, vol. 14, pp. 115 – 120, (2002).
[21] Seth M. Hubbard, Christopher Bailey, Stephen Polly, Ryan Aguinaldo, David Forbes, Ryne Raffaelle, *Proceedings of the 34th PVSC*, Phila., PA, June 6-11th (2009).
[22] S. M. Hubbard, R. Raffaelle, S. Bailey, Nanotechnology for Photovoltaics, USA: CRC Press, 2010, pp. 279-322
[23] A. Luque and A. Marti, Advanced Materials, vol. 22(2), pp. 160-174.
[24] A. Luque, A. Marti, *Phys. Rev. Let.,* vol. 78, pp. 5014-5017, (1997).
[25] P. Harrison, Quantum Wells, Wires, and Dots, 2nd ed., England:2006, pp. 1-12.
[26] P. Harrison, Quantum Wells, Wires, and Dots, 2nd ed., England:2006, pp. 243-267.
[27] D. Bimberg, M. Grundmann, N.N. Ledentiv, Quantum Dot Heterostructures, England: 2001, pp. 115-182.
[28] Q. Xie, P. Chen, and A. Madhukar, *Appl. Phys. Lett.,* vol. 65, p. 2051, (1994).
[29] V. Popescu, G. Bester, and A. Zunger, Physical Review B, vol. 80(4), 2009.
[30] A. Marti, E. Antolin, E. Canovas, N. Lopez, P. G. Linares, A. Luque, C. R. Stanley, and C. D. Farmer, Thin Solid Films, vol. 516(20), pp. 6716-6722, 2008.
[31] A. G. Norman, M. C. Hanna, P. Dippo, D. H. Levi, R. C. Reedy, J. S. Ward, and M. M. Al-Jassim, "InGaAs/GaAs QD superlattices: MOVPE growth, structural and optical characterization, and application in intermediate-band solar cells," in Conference Record of the Thirty-First IEEE Photovoltaic Specialists Conference - 2005, Ieee Photovoltaic Specialists Conference. New York: Ieee, 2005.
[32] C.G. Bailey, S.M. Hubbard, D.V. Forbes, R.P. Raffaelle, *App. Phys. Lett.,* vol. 95, no. 20 (2009).

[33] G. B. Stringfellow, Organometallic Vapor-Phase Epitaxy Theory and Practice, 2d ed., UK:1999. pp. 1-16.
[34] A. Sasaki, Superlattices and Microstructures, vol. 31(2-4), pp. 159, 2002.
[35] N. N. Ledentsov, V. M. Ustinov, V. A. Shchukin, P. S. Kop'ev, Z. I. Alferov, and D. Bimberg, Scs, vol. 32(4), pp. 343-365, 1998.
[36] R. P. Raffaelle, S. Sinharoy, D. M. Wilt, and S. G. Bailey, "Multi-junction solar cell spectral tuning with quantum dots," in Conference Record of the 2006 IEEE 4th World Conference on Photovoltaic Energy Conversion, Vols 1 and 2. New York: Ieee, 2006.
[37] G. S. Solomon, J. A. Trezza, A. F. Marshall, and J. S. Harris, Physical Review Letters, vol. 76(6), pp. 952-955, 1996.
[38] S. M. Hubbard, D. Wilt, S. Bailey, D. Byrnes, and R. Raffaelle, "OMVPE grown InAs quantum dots for application in nanostructured photovoltaics," in Conference Record of the 2006 IEEE 4th World Conference on Photovoltaic Energy Conversion, Vols 1 and 2. New York: Ieee, 2006.
[39] A. D. Yoffe, *Advances In Physic*, vol. 50, pp. 1-208, (2002).
[40] F. Heinrichsdorff, A. Krost, D. Bimberg, A. O. Kosogov, and P. Werner, Applied Surface Science, vol. 123, pp. 725-728, 1998.
[41] J. Y. Marzin, J. M. Gerard, A. Izrael, D. Barrier, and G. Bastard, Physical Review Letters, vol. 73(5), pp. 716-719, 1994.
[42] D. Leonard, K. Pond, and P. M. Petroff, Physical Review B, vol. 50(16), pp. 11687, 1994.
[43] S.M. Sze, K. K. Ng, Physics of Sc Devices, Edition 3, USA: John Wilet & Sons Inc., 2007, pp. 7-62.
[44] "Kottan-Labs Teching", kottan-labs.bgsu.edu, 2001 [Online]. Available: http://kottan-labs.bgsu.edu/teaching/workshop2001/chapter5_files [Accessed: July 21st, 2010].
[45] Y. Okano, M. Shigeta, H. Seto, H. Katahama, S. Nishine,I. Fujimoto, Japanese Journal of Applied Physics, vol. 29, (1991).
[46] G. B. Stringfellow, Organometallic Vapor-Phase Epitaxy Theory and Practice, 2d ed., UK:1999. pp. 391-404.
[47] C. W. Wang, Journal Of Crystal Growth, vol. 203(3), pp. 355-361, 1999.
[48] K. Nakano, S. Tomiya, M. Ukita, H. Yoshida, S. Itoh, E. Morita, M. Ikeda, A. Ishibashi, Journal of Electronic Materials, vol. 25, p. 213, 1996.
[49] Leon, R., Lobo, C., Zou, J., Romeo, T. and Cockayne, D.J.H., 'Stable and metastable InGaAs/GaAs island shapes and surfactant-like suppression of the wetting transformation' Physical Review Letters 81 2486-2489 (1998)
[50] T. Yamamoto, M. Inai, T. Takeba, M. Fujii, K. Kobayashi, Journal of Crystal Growth, vol. 127, p. 865, 1993.
[51] Lobo, R., Leon, R., Liao, Z., Stevens-Kalceff, M.A. and Cockayne, D.J.H., 'Structural evolution and the role of dislocations in InGaAs island formation on GaAs (110) and (111)B surfaces' in "Proc. 14th International Congress on Electron Microscopy" eds. H Benavides and M Yacaman (Institute of Physics, Bristol) pp. 363-364, 1998.
[52] E. Yablonovitch, Journal Of The Optical Society Of America B-Optical Physics, vol. 10(2), pp. 283-295, 1993.
[53] T. H. Gfroerer, "Photoluminescence in Analysis of Surfaces and Interfaces", Encyclopedia of Analytical Chemistry, pp. 9209-9231, 2000.
[54] S.M. Sze, K. K. Ng, Physics of Sc Devices, Edition 3, USA: John Wilet & Sons Inc., 2007, pp. 601-651.
[55] C. W. Wang, Journal Of Crystal Growth, vol. 203(3), pp. 355-361, 1999.
[56] J. S. Hwang, M. F. Chen, K. I. Lin, C. N. Tsai, W. C. Hwang, W. Y. Chou, H. H. Lin, and M. C. Chen, Japanese Journal Of Applied Physics Part 1-Regular Papers Short Notes & Review Papers, vol. 42(9A), pp. 5876-5879, 2003.
[57] F.H. Pollak, H. Shen, *Materials Science & Engineering R-Reports*, vol. 10, no. 7-8, pp. 275-374, (1993).
[58] B. O. Seraphin and N. Bottka, Physical Review, vol. 145(2), pp. 628-&, 1966.
[59] D. E. Aspnes, Surface Science, vol. 37(1), pp. 418-442, 1973.
[60] D. E. Aspnes and J. E. Rowe, Physical Review Letters, vol. 27(4), pp. 188-&, 1971.
[61] T. H. Gfroerer, "Photoluminescence in Analysis of Surfaces and Interfaces", Encyclopedia of Analytical Chemistry, pp. 9209-9231, 2000.
[62] R. Leon and S . Fafard, *Phys. Rev.* ***B*** 58, R1726 (1998).

[63] M. Motyka, G. Sek, R. Kudrawiec, J. Misiewicz, L. H. Li, and A. Fiore, Journal of Applied Physics, vol. 100(7), pp. 073502, 2006.
[64] G. L. Rowland, T. J. C. Hosea, S. Malik, D. Childs, and R. Murray, Applied Physics Letters, vol. 73(22), pp. 3268-3270, 1998.
[65] H. J. Queisser and E. E. Haller, Science, vol. 281(5379), pp. 945-950 1998 August 14, 1998.
[66] G. M. Martin, A. Mitonneau, and A. Mircea, Electronics Letters, vol. 13(7), pp. 191-193, 1977.
[67] P. Chattopadhyay and K. Das, Sc Science And Technology, vol. 8(8), pp. 1605-1610, 1993.
[68] S. C. Binari, P. B. Klein, and T. E. Kazior, Proceedings Of The Ieee, vol. 90(6), pp. 1048-1058, 2002.
[69] J. S. Kim, E. K. Kim, J. O. Kim, S. J. Lee, and S. K. Noh*, Physica Status Solidi B-Basic Solid State Physics*, vol. 246, no. 4, pp. 808-811, (2009).
[70] M. Kaniewska, O. Engstrom, A. Barcz, and M. Pacholak-Cybulska, *Materials Science & Engineering C-Biomimetic And Supramolecular Systems*, vol. 26, no. 5-7, pp. 871-875, (2006).
[71] T. Asano, Z. Fang, and A. Madhukar, *Journal of Applied Physics*, vol.107, (2010).
[72] X. Q. Meng, Z. Q. Chen, P. Jin, Z. G. Wang, and L. Wei, *Applied Physics Letters*, vol. 91, no. 9, (2007).
[73] C. J. Park, H. B. Kim, Y. H. Lee, D. Y. Kim, T. W. Kang, C. Y. Hong, H. Y. Cho, and M. D. Kim, *Journal of Crystal Growth*, vol. 227, pp. 1057-1061, (2001).
[74] H. Y. Cho, *Defects And Diffusion In Scs*, vol. 210-2, (2002).
[75] M. Beguwala and C. R. Crowell, “Characterization of Multiple Deep Level Systems in Sc Junctions by Admittance Measurements,” Solid-State Electron., 17, 203(1 974).
[76] C. Ghezzi, "Space-charge analysis for the admittance of sc junctions with deep impurity levels", Applied Physics A: Materials Science & Processing, vol. 26(3), pp. 191-202, 1981.
[77] D. V. Lang, *Topics in Applied Physics*, vol. 37, pp. 93-133, (1979).
[78] A. Marti, L. Cuadra, and A. Luque, *Physica E*, vol. 14, no. 1-2, pp. 150-157, (2002).
[79] R. Magno, B. R. Bennett, and E. R. Glaser, *Journal of Applied Physics*, vol. 88, no. 10, pp. 5843-5849, (2000).
[80] L. Couture, R. Zitoun, Statistical thermodynamics and properties of matter, Neteherlands: 2000, p. 229.
[81] S.M. Sze, K. K. Ng, Physics of Sc Devices, Edition 3, USA: John Wilet & Sons Inc., 2007, pp. 134-195
[82] J. Nelson, The Physics of Solar Cells, UK: Imperial College Press, 2003, pp. 160-165.
[83] J. Osvald and E. Dobrocka, Sc Science And Technology, vol. 11(8), pp. 1198-1202, 1996.
[84] A. K. Srivastava, B. M. Arora, and S. Guha, Solid-State Electronics, vol. 24(2), pp. 185, 1981.
[85] T. N. Morgan, Physical Review B, vol. 34(4), pp. 2664, 1986.
[86] C. V. Reddy, Y. L. Luo, S. Fung, and C. D. Beling, Physical Review B, vol. 58(3), pp. 1358, 1998.
[87] V. Kazukauskas, E. Kuprusevicius, J. V. Vaitkus, K. M. Smith, S. Nenonen, and A. Owens, "Defect levels and inhomogeneities of high purity high resistivity GaAs films grown by vapour phase epitaxy," in Smart Optical Inorganic Structures And Devices, vol. 4318, Proceedings Of The Society Of Photo-Optical Instrumentation Engineers (Spie). Bellingham: Spie-Int Soc Optical Engineering, 2001.
[88] T. N. Morgan, Physical Review B, vol. 34(4), pp. 2664, 1986.
[89] S. W. Lin, C. Balocco, M. Missous, A. R. Peaker, and A. M. Song, Physical Review B, vol. 72(16), 2005.
[90] J. S. Kim, E. K. Kim, J. O. Kim, S. J. Lee, and S. K. Noh, Physica Status Solidi B-Basic Solid State Physics, vol. 246(4), pp. 808-811, 2009.
[91] R. Leon and S . Fafard, *Phys. Rev.* ***B*** 58, R1726 (1998).
[92] M. Kaniewska, O. Engstrom, A. Barcz, and M. Pacholak-Cybulska, Materials Science & Engineering C-Biomimetic And Supramolecular Systems, vol. 26(5-7), pp. 871-875, 2006.
[93] A. V. Markov, A. Y. Polyakov, N. B. Smirnov, Y. N. Bolsheva, A. V. Govorkov, and B. N. Sharonov, Solid-State Electronics, vol. 46(2), pp. 269-277, 2002.
[94] J. Nishizawa, Y. Oyama, and K. Dezaki, Journal Of Applied Physics, vol. 69(3), pp. 1446-1453, 1991.
[95] N. C. Halder and T. Goodman, Journal Of Vacuum Science & Technology B, vol. 15(6), pp. 2057-2066, 1997.
[96] G. A. Samara, D. W. Vook, and J. F. Gibbons, Journal Of Applied Physics, vol. 71(4), pp. 1807-1814, 1992.